



HAL
open science

Three-dimensional unsteady numerical simulation of a 150 kW full-loop chemical looping combustion pilot with biomass as fuel: A hydrodynamic investigation

Liyan Sun, Enrica Masi, Olivier Simonin, Øyvind Langørgen, Inge Saanum,
Nils Erland L. Haugen

► To cite this version:

Liyan Sun, Enrica Masi, Olivier Simonin, Øyvind Langørgen, Inge Saanum, et al.. Three-dimensional unsteady numerical simulation of a 150 kW full-loop chemical looping combustion pilot with biomass as fuel: A hydrodynamic investigation. *Chemical Engineering Science*, 2022, 260, pp.117835. 10.1016/j.ces.2022.117835 . hal-04533880

HAL Id: hal-04533880

<https://ut3-toulouseinp.hal.science/hal-04533880>

Submitted on 5 Apr 2024

HAL is a multi-disciplinary open access archive for the deposit and dissemination of scientific research documents, whether they are published or not. The documents may come from teaching and research institutions in France or abroad, or from public or private research centers.

L'archive ouverte pluridisciplinaire **HAL**, est destinée au dépôt et à la diffusion de documents scientifiques de niveau recherche, publiés ou non, émanant des établissements d'enseignement et de recherche français ou étrangers, des laboratoires publics ou privés.

Three-dimensional unsteady numerical simulation of a 150 kW_{th} full-loop chemical looping combustion pilot with biomass as fuel: a hydrodynamic investigation.

Liyan Sun^a, Enrica Masi^{a,*}, Olivier Simonin^a, Øyvind Langørgen^b, Inge Saanum^b, Nils Erland L. Haugen^b

^a*Institut de Mécanique des Fluides de Toulouse (IMFT), Université de Toulouse, CNRS, Toulouse, France*

^b*Department of Thermal Energy, SINTEF Energy Research, Trondheim, Norway*

Abstract

A hydrodynamic model for a full Chemical Looping Combustion (CLC) unit was established, and simulations performed using the code NEPTUNE_CFD, which is based on an Euler-Euler approach. The unit is a 150 kW_{th} pilot constructed at SINTEF Energy Research. Three-dimensional unsteady numerical simulations were carried out for studying the local and instantaneous behavior inside the system, and its effect on the mean quantities relevant to the process. Solid volume fraction, mass flow rate and phase velocities were computed and analyzed. Comparison with experimental results showed that the pressure was globally well predicted. Two collision models were also investigated. The agitation between neighboring particles was found to be rather uncorrelated; for this reason, the two collision models led to almost the same results. This work represents a hydrodynamic assessment of CLC using biomass as fuel. It allows to provide insight in the flow within the system, with fairly moderate computational costs.

¹ *Keywords: Chemical Looping Combustion; Fluidized Bed Reactor; CFD; Gas-particles flows;*
² *Eulerian approach.*

3 1. Introduction

⁴ Chemical looping combustion (CLC) is a novel technology for controlling the CO₂ emission
⁵ from combustion processes by separating CO₂ from the combustion products with a very low
⁶ energy penalty (Lyngfelt et al. (2001)). It is viewed as an economic method for CO₂ capturing
⁷ due to the inherent CO₂ separation. A CLC unit mainly comprises a fuel reactor (FR), an
⁸ air reactor (AR), cyclones, loop seals and connecting devices. At pilot scale, CLC reactors are
⁹ mostly designed as two circulating fluidized bed (CFB) reactors (e.g., the 100 kW_{th} unit at
¹⁰ Chalmers (Linderholm et al. (2016)), the 120 kW_{th} unit in Vienna (Pröll et al. (2009)), and the
¹¹ 1 MW_{th} unit in Darmstadt (Ströhle et al. (2014))). The oxygen is transported between reactors
¹² by an oxygen carrier (OC) that is a solid phase exchanging mass, momentum and heat with the
¹³ gas phase. The oxygen carrier reduced in the fuel reactor is regenerated in the air reactor. The
¹⁴ fuel conversion takes place in the fuel reactor where N₂ will not mix with the gaseous products
¹⁵ (Mattisson et al. (2018)). This makes the CO₂ separation possible by condensation of water,

*Corresponding author

Email address: enrica.masi@imft.fr (Enrica Masi)

16 without resorting to any additional separation methods. This inherent feature of the process is
17 the main strength of the CLC technology.

18 Since it was first proposed, the CLC process using gaseous fuel has been widely developed
19 and studied in different forms and by different approaches (Li et al. (2017)), including computa-
20 tional fluid dynamics (Wang et al. (2014); Hamidouche et al. (2019)). For solid fuels, the process
21 is more challenging because it involves many additional mechanisms, including pyrolysis, gasi-
22 fication, unsteady feeding of solid fuels and separation of partially converted fuel particles and
23 oxygen carriers (Lyngfelt (2014)). To improve fuel conversion and ensure efficiency in capturing
24 CO₂, the CLC system may indeed require some changes to accommodate the solid fuel, as the
25 addition of an external carbon stripper (Markström et al. (2013); Abad et al. (2020)), or the
26 realization of new reactor designs (Berguerand and Lyngfelt (2008); Kim et al. (2013); Penthor
27 et al. (2016); Haus et al. (2020)). CLC can also resort to the use of CLOU (chemical-looping
28 with oxygen uncoupling) materials, which improve conversion efficiency thanks to their ability
29 to release oxygen in gas phase (Pérez-Vega et al. (2020)). Several experimental works have
30 been carried out to characterize the behavior of the solid-fuel CLC process (Leion et al. (2008);
31 Ströhle et al. (2015)) and inherent reactions (Cao et al. (2006); Siriwardane et al. (2009); Abad
32 et al. (2011)). The power of existing CLC units range from 500 W_{th} to 3 MW_{th} (Lyngfelt and
33 Linderholm (2017)). Such units use different solid fuels, as coal (Abad et al. (2015)) or biomass
34 (Shen et al. (2009)), together with different oxygen carriers, as ilmenite (Thon et al. (2014)),
35 hematite (Ma et al. (2018)), or manganese ore (Pérez-Astray et al. (2020)), for example. The
36 complexity of the solid-fueled CLC concept makes its modeling and design a real challenge.

37 With the continuous development of supercomputers and their increasing performance, nu-
38 merical approaches are becoming more and more powerful for studying industrial applications
39 at the conception stage or processes that need retrofitting. Nowadays, the Computational Fluid
40 Dynamics (CFD) benefits from High Performance Computing (HPC) systems based on mas-
41 sively parallel architectures, which make its use possible even at industrial scale. In particular,
42 unsteady numerical simulations have the advantage to give access to the local and instanta-
43 neous fields inside the system. This feature makes the unsteady numerical approach very useful
44 to reproduce the characteristics of a process or salient parts of it, providing complementary
45 information to the experimental research. For this reason, numerical studies have increased
46 significantly in recent years, including on CLC technology. An overview of numerical works
47 on CLC is provided by a recent review of Shao et al. (2021). Only some of them concern
48 solid-fueled CLC systems. The 2D numerical simulation, which has successfully been used over
49 the years for reproducing crucial parts of the CLC (see, e.g., Mahalatkar et al. (2011)) or the
50 entire loop (Su et al. (2015)), is leaving the place to the 3D numerical simulation (see May et al.
51 (2018) as an example) which is more representative of the complex structures of the flow due
52 to the three dimensional nature of its behavior (turbulent conditions, loss of symmetry close to
53 injections, etc.). Concerning full-loop solid-fueled reactive CLC, three-dimensional studies have
54 become available in the literature (Parker (2014); Reinking et al. (2019)) but still few of them
55 assess the numerical results compared to experimental measurements (Chen et al. (2019)).

56 It is well known that hydrodynamics strongly affects the reactive predictions. The reason is
57 that characteristic reaction times are usually very large compared to those of the flow evolution
58 or momentum transfers in this type of process (in absence of CLOU materials). This is why
59 cold flow models are frequently employed to characterize the CLC behavior, before moving
60 on to ultimate reactive conditions. The increased complexity of the flow when working with
61 solid fuels makes hydrodynamic investigations even more useful in a first stage. Examples
62 of numerical studies based on full-loop cold-flow CLC are the recent works of Wang et al.
63 (2020a) and Wang et al. (2020b), who studied the hydrodynamics of CLC units conceived

64 to be used with coal as fuel, with inherent separation or gasification systems. Their studies
65 focused, respectively, on the investigation of the separation (coal from OC) particle efficiency
66 by the high-flux carbon stripper integrated into the process, and on the characterization of the
67 flow in gasifier and reduction reactors, depending on the operating conditions. Results were
68 validated by comparing with previous experimental investigations from the same laboratory.
69 Another example of cold-flow CLC investigation is the three-dimensional numerical simulation
70 carried out by [Shao et al. \(2020\)](#), who analyzed a novel two-stage air reactor and its response
71 under different operating conditions on the whole CLC behavior. Results about the pressure
72 predictions were validated against experimental data.

73 In the present work, we also explore the hydrodynamics of a full-loop solid-fueled CLC, but
74 comparing pressure predictions with experimental measurements from a hot instead of a cold
75 experimental unit. The hot unit is a 150 kW_{th} pilot operating at SINTEF Energy Research
76 (Trondheim, Norway). The 3D unsteady numerical simulations are performed using an Euler-
77 Euler approach. The latter is considered for its efficiency and low computational costs. In fact,
78 in an Euler-Euler approach, most of the efforts are spent on the development and validation of
79 the modeling to account for additional physical effects (as, for example, particle rotation with
80 friction ([Goniva et al. \(2012\)](#)) or triboelectric charging ([Kolehmainen et al. \(2018\)](#); [Montilla
81 et al. \(2020\)](#))), as well as on the numerical implementation in industrial codes. Depending
82 on the particle characteristics and dimensions at industrial scale, a filtered formulation or
83 heterogeneity models may also be needed ([Schneiderbauer and Pirker \(2014\)](#)). But in the end,
84 the result is an approach that is not excessively time consuming, unless to solve for a distribution
85 of particle sizes, and that has the numerical advantage of treating the separate sets of phase
86 equations analogously, which allows a strong, potentially implicit, coupling between the phases,
87 implying a true mathematical convergence rate with respect to the mesh size and time step.

88 The alternative Euler-Lagrange particle approaches, such as the Discrete Element Method
89 (CFD-DEM) ([Cundall and Strack \(1979\)](#); [Tsuji et al. \(1993\)](#)), have modeling advantages (easier
90 implementation of additional physical aspects such as polydispersion, particle rotation, particle-
91 particle friction, non-spherical shape, etc.) and numerical advantages (for example non-diffusive
92 Lagrangian numerical schemes leading to less sensitivity to the mesh size), but they are hugely
93 expensive in terms of computational costs already at pilot scale, and definitely unusable at
94 industrial scale. Emerging alternative methods are the Euler-Lagrange approaches using parcels
95 instead of particles ([Pirker et al. \(2010\)](#)), directly accounting for collisions between parcels and
96 at the wall (an overview is given in the review of [Di Renzo et al. \(2021\)](#)), or modeling collisions on
97 a continuum basis (see, e.g., [Snider \(2001\)](#); [Cloete et al. \(2012\)](#)). Unlike a CFD-DEM approach
98 where particles are tracked individually, Euler-Lagrange approaches using parcels need additional
99 assumptions to model mechanisms acting on the particles, which are not taken directly into
100 account (such as solids contacts). These approaches are promising and offer an affordable
101 alternative to the Eulerian models, for example in polydisperse flows when applications require
102 to account for several particle sizes. Depending on the model, they can also provide accuracy
103 improvement, especially in regimes with fine clusters and large-scale crossing ([Cloete et al.
104 \(2012\)](#)). However, efforts still have to be made to reach a degree of maturity equivalent to the
105 Euler-Euler methods. For this reason, an Euler-Euler approach still remains the most reliable
106 and competitive in dense (or moderately dense) regimes; this is why it was considered for this
107 work.

108 The numerical simulations performed in this study use a non-reactive isothermal model.
109 The model considers fuel and OC conversion by accounting for additional gas injection due to
110 the products from the full fuel conversion and redox reactions. The OC flow behavior inside the
111 reactors and the effect of the coupling of the two reactors are analyzed to improve understanding

112 of the CLC system. The results obtained from these numerical simulations should help in the
 113 design and operation of CLC units.

114 2. Numerical approach and mathematical modeling

115 Unsteady 3D numerical simulations of the CLC unit are carried out using the N-Euler ap-
 116 proach for gas-solid turbulent flows implemented in NEPTUNE_CFD by IMFT (Institut de
 117 Mécanique des fluides de Toulouse), in collaboration with EDF (Electricité de France) R&D
 118 (Hamidouche et al. (2018), Neau et al. (2020)). NEPTUNE_CFD is a multiphase CFD code de-
 119 veloped in the framework of the NEPTUNE project, financially supported by EDF, CEA (Com-
 120 missariat à l'Énergie Atomique), IRSN (Institut de Radioprotection et de Sécurité Nucléaire) and
 121 Framatome. The code solves the coupled partial differential equations by a finite-volume ap-
 122 proach using an adaptive time step determined by a CFL (Courant–Friedrichs–Lewy) criterion
 123 for each phase. The solver is based on a cell-center type finite volume method and an elliptic
 124 fractional time-step method. The latter relies on an alpha-pressure cycle (alpha stands for phase
 125 volume fraction), which is an iterative method to ensure mass and energy conservation. First,
 126 at the beginning of each substep, the velocity is predicted for each phase without accounting for
 127 volume fraction and pressure variations in time, while accounting for inter-phase coupling by
 128 using an implicit formulation during the sub-step iterations. Then, mass and energy equations
 129 are integrated enforcing conservativity, and the velocity is corrected by accounting for volume
 130 fraction and pressure variations. Then, the pressure is computed by solving an elliptic equa-
 131 tion and the velocities are corrected with respect to the pressure time increment. Convergence
 132 criteria of the alpha-pressure cycling is based on the condition of volume conservation of the
 133 mixture (EDF R&D (2017)). The code is characterized by a calculation of co-localized gradients
 134 with reconstruction methods and a distributed-memory parallelism by domain decomposition
 135 (MPI parallelization). It uses unstructured meshes with all cell types and connections. Further
 136 details about the numerical code can be found in Neau et al. (2020).

137 In the present work, the multiphase N-Euler approach implemented in NEPTUNE_CFD has
 138 been used to model the evolution of both the gas and solid phase under isothermal conditions.
 139 In this section, the corresponding mathematical modeling is presented. More details about the
 140 approach may be found in the work of Simonin (2000).

141 In the current study, a non-reactive isothermal hydrodynamic investigation is carried out.
 142 On this basis, the mass balance equations are written as follows:

$$\frac{\partial(\alpha_g \rho_g)}{\partial t} + \frac{\partial(\alpha_g \rho_g U_{g,j})}{\partial x_j} = 0, \quad (1)$$

$$\frac{\partial(\alpha_s \rho_s)}{\partial t} + \frac{\partial(\alpha_s \rho_s U_{s,j})}{\partial x_j} = 0, \quad (2)$$

144 where ρ , α and U are mean density, volume fraction and velocity, respectively. The subscripts
 145 g represents the gas phase while s stands for the solid phase. Since reactions are not taken into
 146 consideration in the current work, source terms related to the mass transfer are set to zero.

147 The momentum equations are given by:

$$\alpha_g \rho_g \left(\frac{\partial U_{g,i}}{\partial t} + U_{g,j} \frac{\partial U_{g,i}}{\partial x_j} \right) = -\alpha_g \frac{\partial P_g}{\partial x_i} + \alpha_g \rho_g g_i + I_{s \rightarrow g,i} + \frac{\partial \sum_{g,ij}}{\partial x_j}, \quad (3)$$

$$\alpha_s \rho_s \left(\frac{\partial U_{s,i}}{\partial t} + U_{s,j} \frac{\partial U_{s,i}}{\partial x_j} \right) = -\alpha_s \frac{\partial P_g}{\partial x_i} + \alpha_s \rho_s g_i + I_{g \rightarrow s,i} + \frac{\partial \sum_{s,ij}}{\partial x_j}. \quad (4)$$

149 In the above equations, P_g is the gas pressure and $I_{g \rightarrow s}(= -I_{s \rightarrow g})$ is the mean gas to solid
 150 interphase momentum transfer after subtracting the mean gas pressure gradient contribution
 151 (Archimedes' force). It will be detailed later. $\sum_{,ij}$ are stress tensors defined as:

$$\sum_{g,ij} = -\alpha_g \rho_g \langle u''_{g,i} u''_{g,j} \rangle_g + \Theta_{g,ij} = -\alpha_g \rho_g R_{g,ij} + \Theta_{g,ij}, \quad (5)$$

$$\sum_{s,ij} = -\alpha_s \rho_s \langle u''_{s,i} u''_{s,j} \rangle_s + \Theta_{s,ij} + \phi_{s,ij} = -\alpha_s \rho_s R_{s,ij} + \Theta_{s,ij} + \phi_{s,ij}, \quad (6)$$

153 where $u''_i = u_i - U_i$.

154 For the gas phase, $R_{g,ij}$ and $\Theta_{g,ij}$ represent the turbulent-Reynolds and viscous stress tensors.
 155 They are written as:

$$R_{g,ij} = -\nu_g^t \left(\frac{\partial U_{g,i}}{\partial x_j} + \frac{\partial U_{g,j}}{\partial x_i} \right) + \frac{2}{3} \delta_{ij} \left(k + \nu_g^t \frac{\partial U_{g,m}}{\partial x_m} \right), \quad (7)$$

$$\Theta_{g,ij} = \alpha_g \mu_g \left(\frac{\partial U_{g,i}}{\partial x_j} + \frac{\partial U_{g,j}}{\partial x_i} - \frac{2}{3} \frac{\partial U_{g,m}}{\partial x_m} \delta_{ij} \right), \quad (8)$$

157 where δ_{ij} is the Kronecker delta. k and μ_g are turbulent kinetic energy and laminar dynamic
 158 viscosity, respectively. ν_g^t is the turbulent kinematic viscosity written as (Vermorel et al. (2003))

$$\nu_g^t = \frac{2}{3} k \tau_g^t \left[1 + C_{12} \frac{\alpha_s \rho_s \tau_{gs}^t}{\alpha_g \rho_g \tau_{gs}^F} \left(1 - \frac{q_{gs}}{2k} \right) \right]^{-1}, \quad (9)$$

160 where the constant $C_{12} = 0.34$. The quantity q_{gs} is the fluid-particle velocity covariance and it
 161 will be presented later with the solid phase. τ_{gs}^t and τ_{gs}^F are timescales related to the interaction
 162 between the gas and the solid phases. The eddy-particle interaction time is the characteristic
 163 time for the gas turbulence seen by the particles (Simonin et al. (1993)):

$$\tau_{gs}^t = \frac{\tau_g^t}{\sigma_k} \left(1 + C_\beta \frac{V_{r,i} V_{r,i}}{\frac{2}{3} k} \right)^{-1/2}, \quad (10)$$

164 and τ_{gs}^F is the mean particle relaxation time (detailed later). The fluid turbulent timescale is
 165 defined as $\tau_g^t = C_\mu \frac{3k}{2\varepsilon}$. A $k - \varepsilon$ model is adopted for closing the above equations. According
 166 to this model (Vermorel et al. (2003)), the transport equations for the gas turbulent kinetic
 167 energy and dissipation rate are written as:

$$\alpha_g \rho_g \left(\frac{\partial k}{\partial t} + U_{g,j} \frac{\partial k}{\partial x_j} \right) = \frac{\partial}{\partial x_j} \left(\alpha_g \rho_g \frac{\nu_g^t}{\sigma_k} \frac{\partial k}{\partial x_j} \right) - \alpha_g \rho_g R_{g,ij} \frac{\partial U_{g,i}}{\partial x_j} - \alpha_g \rho_g \varepsilon + \Pi_{s \rightarrow g}^k, \quad (11)$$

$$\alpha_g \rho_g \left(\frac{\partial \varepsilon}{\partial t} + U_{g,j} \frac{\partial \varepsilon}{\partial x_j} \right) = \frac{\partial}{\partial x_j} \left(\alpha_g \rho_g \frac{\nu_g^t}{\sigma_\varepsilon} \frac{\partial \varepsilon}{\partial x_j} \right) - \alpha_g \rho_g C_{\varepsilon 1} \frac{\varepsilon}{k} R_{g,ij} \frac{\partial U_{g,i}}{\partial x_j} - \alpha_g \rho_g C_{\varepsilon 2} \frac{\varepsilon^2}{k} + \Pi_{s \rightarrow g}^\varepsilon, \quad (12)$$

169 where $\Pi_{s \rightarrow g}^k$ and $\Pi_{s \rightarrow g}^\varepsilon$ account for the effect of the solid phase on the gas turbulence. Assuming
 170 that particle size is comparable or less than the Kolmogorov length scale, the interphase terms
 171 are given by

$$\Pi_{s \rightarrow g}^k = \frac{\alpha_s \rho_s}{\tau_{gs}^F} (-2k + q_{gs} + V_{d,i} V_{r,i}), \quad (13)$$

172 and

$$\Pi_{s \rightarrow g}^\varepsilon = C_{\varepsilon 3} \frac{\varepsilon}{k} \Pi_{s \rightarrow g}^k, \quad (14)$$

173 using the relative velocity

$$V_{r,i} = (U_{s,i} - U_{g,i}) - V_{d,i}, \quad (15)$$

174 and accounting for the turbulent drift velocity (Simonin et al. (1993))

$$V_{d,i} = -D_{gs}^t \left(\frac{1}{\alpha_s} \frac{\partial \alpha_s}{\partial x_i} - \frac{1}{\alpha_g} \frac{\partial \alpha_g}{\partial x_i} \right). \quad (16)$$

175 The constants involved in the $k - \varepsilon$ model are $C_\mu = 0.09$, $C_{\varepsilon 1} = 1.44$, $C_{\varepsilon 2} = 1.92$, $C_{\varepsilon 3} = 1.2$,
176 $\sigma_k = 1.0$ and $\sigma_\varepsilon = 1.3$.

177 For the solid phase, the effective stress tensor (Eq. 6) comprises a kinetic part, $R_{s,ij}$,
178 which is dominant in dilute flow, and a collisional part, $\Theta_{s,ij}$, which is dominant in dense flow.
179 Also the frictional part, $\phi_{s,ij}$, contributes to the effective stress tensor in zones with very high
180 concentration and long solid-solid contact. The kinetic and collisional contributions of the
181 effective particle stress tensor are written, respectively, as (Boelle et al. (1995); Gobin et al.
182 (2003); Jenkins and Richman (1986); Simonin (2000))

$$R_{s,ij} = -\nu_s^{kin} \left(\frac{\partial U_{s,i}}{\partial x_j} + \frac{\partial U_{s,j}}{\partial x_i} \right) + \frac{2}{3} \delta_{ij} \left(q_s^2 + \nu_s^{kin} \frac{\partial U_{s,m}}{\partial x_m} \right), \quad (17)$$

183

$$\Theta_{s,ij} = - \left[\frac{2}{3} \alpha_s \rho_s q_s^2 2\alpha_s g_0 (1 + e_c) - \Lambda_s \frac{\partial U_{s,m}}{\partial x_m} \right] \delta_{ij} + \alpha_s \rho_s \nu_s^{col} \left(\frac{\partial U_{s,i}}{\partial x_j} + \frac{\partial U_{s,j}}{\partial x_i} - \frac{2}{3} \frac{\partial U_{s,m}}{\partial x_m} \delta_{ij} \right). \quad (18)$$

184 In the above equations, e_c is the normal restitution coefficient, g_0 is the radial distribution
185 function, ν_s^{kin} is the particle kinetic viscosity, and ν_s^{col} represents the particle collisional viscosity:

186

$$\nu_s^{kin} = \left[\nu_{gs}^t + \frac{\tau_{gs}^F}{2} \frac{2}{3} q_s^2 (1 + \alpha_s g_0 \Phi_c) \right] \left(1 + \frac{\tau_{gs}^F}{2} \frac{\sigma_c}{\tau_s^c} \right)^{-1} \quad (19)$$

187

$$\nu_s^{col} = \frac{4}{5} \alpha_s g_0 (1 + e_c) \left(\nu_s^{kin} + d_s \sqrt{\frac{2}{3} \frac{q_s^2}{\pi}} \right). \quad (20)$$

188 Λ_s , in Eq.18, is defined as:

$$\Lambda_s = \alpha_s \rho_s \frac{4}{3} \alpha_s g_0 (1 + e_c) d_s \sqrt{\frac{2}{3} \frac{q_s^2}{\pi}} \quad (21)$$

189 The particle fluctuant kinetic energy, q_s^2 , is defined as $q_s^2 = \langle u''_{s,i} u''_{s,i} \rangle_s / 2$. The transport equation
190 of q_s^2 is

$$\alpha_s \rho_s \left(\frac{\partial q_s^2}{\partial t} + U_{s,j} \frac{\partial q_s^2}{\partial x_j} \right) = \frac{\partial}{\partial x_j} \left(\alpha_s \rho_s \kappa_s^{eff} \frac{\partial q_s^2}{\partial x_j} \right) + \sum_{s,ij} \frac{\partial U_{s,i}}{\partial x_j} - \alpha_s \rho_s \varepsilon_s + \Pi_{q_s}, \quad (22)$$

191 where κ_s^{eff} is the particle effective diffusivity coefficient, $\kappa_s^{eff} = \kappa_s^{kin} + \kappa_s^{col}$, formed by the
192 following contributions:

$$\kappa_s^{kin} = \left[\frac{1}{3} \tau_{gs}^t q_{gs} + \frac{5}{9} \tau_{gs}^F \frac{2}{3} q_s^2 (1 + \alpha_s g_0 \varphi_c) \right] \left(1 + \frac{5}{9} \tau_{gs}^F \frac{\xi_c}{\tau_s^c} \right)^{-1} \quad (23)$$

193

$$\kappa_s^{col} = \alpha_s g_0 (1 + e_c) \left[\frac{6}{5} \kappa_s^{kin} + \frac{4}{3} d_s \sqrt{\frac{2}{3} \frac{q_s^2}{\pi}} \right]. \quad (24)$$

194

$$\varphi_c = \frac{3}{5} (1 + e_c)^2 (2e_c - 1) \quad (25)$$

195 and

$$\xi_c = \frac{(1 + e_c)(49 - 33e_c)}{100} \quad (26)$$

196 ε_s , in Eq.22, is the particle kinetic energy dissipation rate due to the inelastic collisions (Simonin
197 et al. (2002)):

$$\varepsilon_s = \frac{1}{3} (1 - e_c^2) \frac{\delta q_s^2}{\tau_s^c}. \quad (27)$$

198 where δq_s^2 represents the uncorrelated part of the random particle kinetic energy, also named
199 granular temperature ($\Theta_s = 2/3 \delta q_s^2$) (Fox (2014)). Π_{q_s} , in Eq. (22), is the interphase turbulent
200 kinetic energy transfer rate and is written as

$$\Pi_{q_s} = -\alpha_s \rho_s \frac{1}{\tau_{gs}^F} (2q_s^2 - q_{gs}), \quad (28)$$

201 where $q_{gs} = \langle u''_{g,i} u''_{s,i} \rangle_s$ is the fluid-particle velocity covariance, which is solved by the following
202 transport equation (Simonin (2000))

$$\alpha_s \rho_s \left(\frac{\partial q_{gs}}{\partial t} + \partial U_{s,j} \frac{\partial q_{gs}}{\partial x_j} \right) = \frac{\partial}{\partial x_j} \left(\alpha_s \rho_s \frac{\nu_{gs}^t}{\sigma_k} \frac{\partial q_{gs}}{\partial x_j} \right) - \alpha_s \rho_s \varepsilon_{gs} + \Pi_{q_{gs}} - \alpha_s \rho_s \left[\langle u''_{g,i} u''_{s,j} \rangle_s \frac{\partial U_{s,i}}{\partial x_j} + \langle u''_{g,j} u''_{s,i} \rangle_s \frac{\partial U_{g,i}}{\partial x_j} \right], \quad (29)$$

203 where ε_{gs} is the fluid-particle covariance dissipation rate due to viscous dissipation and crossing
204 trajectory effects, which is modeled as:

$$\varepsilon_{gs} = \frac{q_{gs}}{\tau_{gs}^t}. \quad (30)$$

205 The interphase interaction term, $\Pi_{q_{gs}}$, is written as:

$$\Pi_{q_{gs}} = -\alpha_s \rho_s \frac{1}{\tau_{gs}^F} \left[(q_{gs} - 2k) + \frac{\alpha_s \rho_s}{\alpha_g \rho_g} (q_{gs} - 2\tilde{q}_s^2) \right]. \quad (31)$$

206 where \tilde{q}_s^2 is the correlated part of the random part kinetic energy defined later. The first
207 contribution on the right-hand side of the above equation, proportional to $(q_{gs} - 2k)$, represents
208 the effect of particle entrainment by gas turbulence and is dominant, and generally positive,
209 in dilute flows ($2k > q_{gs}$). The second term, proportional to $(q_{gs} - 2\tilde{q}_s^2)$, represents the effect of
210 two-way coupling by particle agitation and is dominant and generally negative ($2\tilde{q}_s^2 < q_{gs}$), in
211 high solid mass loaded flows.

212 The frictional tensor, $\phi_{s,ij}$, in Eq. (6), is defined according to the frictional model (Bennani
213 et al. (2017)):

$$\phi_{s,ij} = 2\mu_s^{fr} D_{s,ij} - P_s^{fr} \delta_{ij}. \quad (32)$$

214 $D_{s,ij}$ is the particle shear tensor written as:

$$D_{s,ij} = \frac{1}{2} \left[\frac{\partial U_{s,i}}{\partial x_j} + \frac{U_{s,j}}{\partial x_i} - \frac{2}{3} \frac{\partial U_k}{\partial x_k} \delta_{ij} \right]. \quad (33)$$

215 The frictional pressure, P_s^{fr} , is modeled according to Johnson and Jackson (1987) and Johnson
216 et al. (1990):

$$P_s^{fr} = \begin{cases} Fr \frac{(\alpha_s - \alpha_s^{min})^r}{(\alpha_s^{max} - \alpha_s)^s}; & \alpha_s > \alpha_s^{min} \\ 0; & else \end{cases} \quad (34)$$

217 where $Fr = 0.05$, $r = 2$ and $s = 5$ are model parameters, which may be varied depending on
 218 the types of particles. In this work, α_s^{min} is set equal to 0.55, which is an appropriate value for
 219 spherical particles. The frictional viscosity is modeled as follows (Srivastava and Sundaresan
 220 (2003); Bennani et al. (2017)):

$$\mu_s^{fr} = \begin{cases} Fr \frac{\sqrt{2} P_p^{fr} \sin(\eta)}{2\sqrt{D_{s,ij} D_{s,ij} + \psi}}; & \alpha_s > \alpha_s^{min} \\ 0; & else \end{cases} \quad (35)$$

221 where η is the internal friction angle (25°) and $\psi = 2/3(q_s^2/d_s^2)$. The interphase momentum
 222 transfer between gas and solid after subtraction of the gas pressure gradient effect is written
 223 as:

$$I_{s \rightarrow g, i} = -I_{g \rightarrow s, i} = \alpha_s \rho_s \frac{1}{\tau_{gs}^F} V_{r, i} \quad (36)$$

224 on the basis of the mean relative velocity and the mean particle relaxation time, τ_{gs}^F , which
 225 accounts for the drag effect on the particles:

$$\frac{1}{\tau_{gs}^F} = \frac{3\rho_g \langle |v_r| \rangle_s}{4\rho_s d_s} C_D. \quad (37)$$

226 This time is expressed using two different experimental laws, Wen and Yu and Ergun's law,
 227 according to the modeling proposed by Gobin et al. (2003):

$$C_D = \begin{cases} C_{D, WY}; & \alpha_g \geq 0.7 \\ \min[C_{D, WY}; C_{D, Erg}]; & \alpha_g < 0.7 \end{cases} \quad (38)$$

228 with

$$C_{D, Erg} = 200 \frac{1 - \alpha_g}{Re_p} + \frac{7}{3} \quad (39)$$

$$C_{D, WY} = \begin{cases} \frac{24}{Re_p} [1 + 0.15 Re_p^{0.687}] \alpha_g^{-1.7}; & Re_p < 1000 \\ 0.44 \alpha_g^{-1.7}; & Re_p \geq 1000 \end{cases} \quad (40)$$

230 Here, Re_p is the particle Reynolds number defined as

$$Re_p = \frac{\alpha_g \rho_g \langle |v_r| \rangle_s d_s}{\mu_g}. \quad (41)$$

231 Finally, τ_s^c is the inter-particle collision time :

$$\tau_s^c = \left(6 \frac{\alpha_s g_0}{d_s} \sqrt{\frac{16}{\pi} \frac{2}{3} \delta q_s^2} \right)^{-1}. \quad (42)$$

232 In this study, two different models are used for the uncorrelated contribution of the random
 233 kinetic energy in the inter-particle collision time (Equation (42)) and in the kinetic energy
 234 dissipation by inelastic collision (Equation (27)). Indeed, according F evrier et al. (2005) and
 235 Fox (2014), we may assume that the random particle kinetic energy q_s^2 may be separated in
 236 two parts:

$$q_s^2 = \tilde{q}_s^2 + \delta q_s^2 \quad (43)$$

237 where \tilde{q}_s^2 is the correlated contribution, representing the collective fluctuating motion of the
 238 particles, and δq_s^2 is the uncorrelated contribution, representing the particle-particle relative

239 fluctuating motion (Simonin et al. (2002)). For the uncorrelated model, the correlation effect
 240 of the neighboring particles is not taken into consideration and we get the following assumption:

$$241 \quad \begin{cases} \tilde{q}_s^2 = 0 \\ \delta q_s^2 = q_s^2 \end{cases} \quad (44)$$

242 Such an assumption is corresponding to classic kinetic theory of granular flow (Gidaspow
 243 (1994)). For the correlated model, according to the works of Laviéville et al. (1995) and
 244 Simonin et al. (2002), it can be expressed as :

$$\begin{cases} \tilde{q}_s^2 = \zeta_{gs}^2 q_s^2 \\ \delta q_s^2 = [1 - \zeta_{gs}^2] q_s^2 \end{cases} \quad (45)$$

245 where ζ_{gs}^2 represents a correlation coefficient and is written as

$$\zeta_{gs}^2 = \frac{[q_{gs}]^2}{4kq_s^2}, \quad 0 < \zeta_{gs}^2 < 1. \quad (46)$$

246 The correlated model will account for correlation between colliding particles due to the inter-
 247 action with the fluid turbulence (Février et al. (2005)). When an uncorrelated assumption is
 248 used, \tilde{q}_s^2 in Equation (31) turns to zero, and the contribution of two-way coupling to the inter-
 249 phase term is a destruction term directly proportional to the fluid-particle velocity covariance.
 250 When a correlated model is used, this contribution is obtained from the total particle kinetic
 251 energy, using the above correlation coefficient (Simonin et al. (2002)). We can notice that ac-
 252 cording to Equations (45) and (46), we may write, $q_{gs} - 2\tilde{q}_s^2 = q_{gs}(1 - q_{gs}/2k)$ showing that the
 253 sign of the two-way contribution is directly depending on the ratio between the fluid-particle
 254 velocity covariance and the fluid turbulent kinetic energy. In addition, when the value of ζ_{gs}^2
 255 tends towards zero, that is for very large Stokes numbers in particle-laden turbulent flows, the
 256 correlated model reverts to the uncorrelated one.

257 3. Experimental system and simulation setup

258 In this work, a double-loop CFB reactor system, corresponding to the experimental facility
 259 at SINTEF Energy Research (Trondheim, Norway), is adopted to investigate the hydrodynam-
 260 ics of the CLC unit. Two reactors, two cyclones, two loop seals and one lifter are designed and
 261 built for this facility, which has also been used to study CLC of gaseous fuels (Langørgen et al.
 262 (2017)). The operating schematic diagram is displayed in Figure 1. The dimensions of the CLC
 263 unit are reported in Table 1. In the experiments, ilmenite from Titania A/S in Norway (of bulk
 264 density 2600 kg/m³ and mean diameter (D_{50}) 90 μm) is used as oxygen carrier.

265 In the numerical simulation, the system is meshed by an O-grid method with approximately
 266 0.7 million cells (the reference case), which is a suitable compromise between fine and coarse
 267 mesh considering both accuracy and calculation costs. No-slip or free-slip wall boundary con-
 268 ditions for the mean particle velocity and zero-flux boundary conditions for the particle kinetic
 269 energy are imposed (Fede et al. (2016)). Friction conditions are used for the gas phase, accord-
 270 ing to the $k - \varepsilon$ modeling considered in this work. The operating temperature is set to 1273 K,
 271 according to the experiments. An overview of the CLC mesh is given in Figure 2.

272 Mass inventories are calculated from the experimental pressure-drop measurements, and
 273 are summarized in the Table 2. In the experiments, each loop seal was designed with three
 274 chambers: central, external and internal. The particles separated by the cyclone enter the

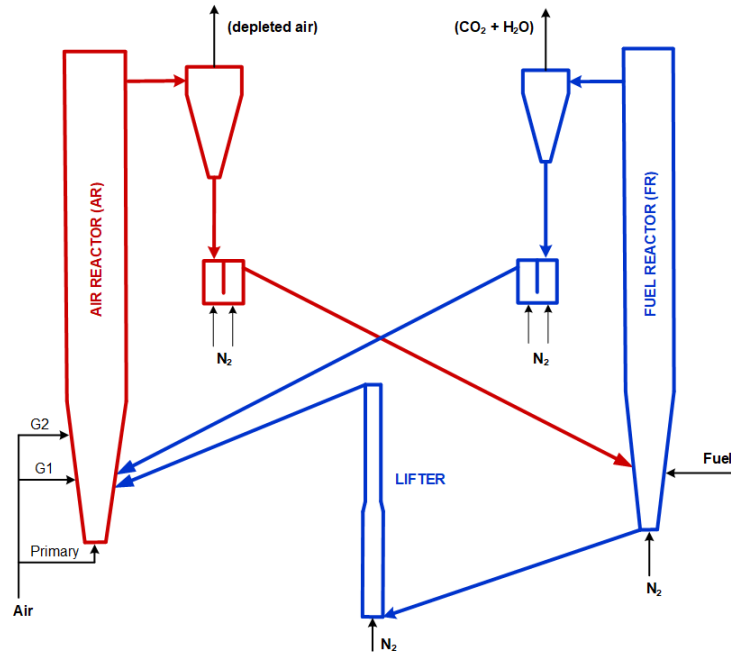


Figure 1: Scheme of the 150 kW_{th} chemical looping combustion pilot at SINTEF, Norway.

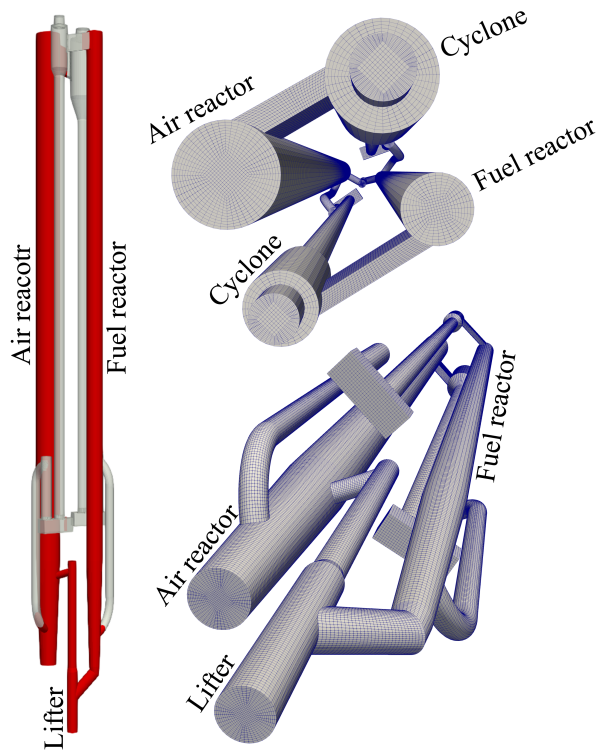


Figure 2: Structure of the 150 kW_{th} chemical looping combustion pilot at SINTEF and mesh plan.

275 central part of the loop seal. Then, the particles are transported to the other reactor through the
 276 external chamber, or re-circulated back into the original reactor through the internal chamber.
 277 For the current CLC experiments, the particle outlet leg connected with the internal chamber
 278 was shut down. For this reason, in the numerical simulation only the central and external
 279 chambers were considered (as shown in Figure A.22 for the FR loop seal). Therefore, only two
 280 third of the mass inventory of each loop seal was taken into account, in addition to the mass

Table 1: Dimension of the CLC unit.

| Item | Value | Units |
|-----------------------------------------|-------|-------|
| Height of AR | 6.0 | m |
| Inner diameter of AR (cylindrical part) | 23.0 | cm |
| Height of the AR conical part | 1.0 | m |
| Bottom diameter of the AR conical part | 15.0 | cm |
| Height of FR (including lifter) | 6.7 | m |
| Inner diameter of FR (cylindrical part) | 15.4 | cm |
| Height of the FR conical part | 1.0 | m |
| Bottom diameter of the FR conical part | 10.0 | cm |

Table 2: Mass inventories.

| Item | Value | Units |
|--------------|--------------|-------|
| Air reactor | 18.1 | kg |
| Fuel reactor | 28.2 | kg |
| Lifter | 11.5 | kg |
| AR loop seal | 52.1 (37.7) | kg |
| FR loop seal | 42.4 (30.4) | kg |
| Total | 152.3(125.9) | kg |

281 of the particles contained in each connecting pipe. These values are shown in parentheses in
 282 Table 2.

283 At the initial time, the solid phase is initialized by a solid volume fraction of 0.55, the particle
 284 diameter is set to 90 μm and the particle density to 4727 kg/m^3 (reference case), corresponding
 285 to a mean voidage of 0.45 (cf. Section 4.4). Particle diameter and particle density are kept
 286 constant during the numerical simulation. The initial mass distribution in the CLC is set
 287 according to the experiments (cf. previous discussion), which is beneficial for shortening the
 288 computational time to reach a steady state.

289 In this study, only one solid phase is considered, the oxygen carrier, while the biomass is
 290 taken into account through its end products. Moreover, to estimate as best as possible the
 291 amount of gases in the system, the mass transfer of oxygen, from the solid in the fuel reactor,
 292 and to the solid in the air reactor, is considered as well. Three different ways of injection are
 293 tested. The numerical strategy to account for the change in gas flow rate due to reactions is
 294 detailed below.

295 The biomass is composed of volatiles, char and ash. Volatiles are released into the fuel
 296 reactor and take part in OC reduction reactions. Gas products and a part of volatiles are
 297 involved in char gasification reactions. Assuming complete reactions in the fuel reactor, and a
 298 statistically stationary state, one may estimate the mass flow rate of the whole mixture from
 299 the mass flow rate of the final products, CO_2 and H_2O , defined as

$$\dot{Q}_{\text{CO}_2} = \dot{Q}_{\text{bio}} Y_{\text{vol}} X_{\text{CO}_2} + \dot{Q}_{\text{bio}} Y_{\text{vol}} X_{\text{CO}} \frac{W_{\text{CO}_2}}{W_{\text{CO}}} + \dot{Q}_{\text{bio}} Y_{\text{vol}} X_{\text{CH}_4} \frac{W_{\text{CO}_2}}{W_{\text{CH}_4}} + \dot{Q}_{\text{bio}} Y_{\text{char}} \frac{W_{\text{CO}_2}}{W_{\text{char}}}, \quad (47)$$

300

$$\dot{Q}_{\text{H}_2\text{O}} = \dot{Q}_{\text{bio}} Y_{\text{vol}} X_{\text{H}_2\text{O}} + \dot{Q}_{\text{bio}} Y_{\text{vol}} X_{\text{H}_2} \frac{W_{\text{H}_2\text{O}}}{W_{\text{H}_2}} + \dot{Q}_{\text{bio}} Y_{\text{vol}} X_{\text{CH}_4} \frac{2W_{\text{H}_2\text{O}}}{W_{\text{CH}_4}}, \quad (48)$$

301 where \dot{Q}_{bio} is the injection mass flow rate (kg/s) of biomass, Y_{vol} is the mass fraction of volatiles,
 302 and Y_{char} the mass fraction of char ($Y_{vol} + Y_{char} = 1 - Y_{ash}$). X_{β} is the mass fraction of the
 303 species β in the volatiles ($\sum_{\beta} X_{\beta} = 1$). The values of Y_{vol} (0.845) and Y_{char} (0.15), as well as
 304 the volatile composition ($X_{CO} = 0.5581$, $X_{CO_2} = 0.1594$, $X_{CH_4} = 0.1926$, $X_{H_2} = 0.0183$, and
 305 $X_{H_2O} = 0.0716$) are obtained from proximate analysis and heat and mass balance (Thunman
 306 et al. (2001)), assuming these five species as the primary volatiles. The mass flow rate of oxygen
 307 required to full conversion in the fuel reactor is therefore

$$\dot{Q}_{O_2} = \dot{Q}_{bio} Y_{vol} X_{CO} \frac{0.5W_{O_2}}{W_{CO}} + \dot{Q}_{bio} Y_{vol} X_{H_2} \frac{0.5W_{O_2}}{W_{H_2}} + \dot{Q}_{bio} Y_{vol} X_{CH_4} \frac{2W_{O_2}}{W_{CH_4}} + \dot{Q}_{bio} Y_{char} \frac{W_{O_2}}{W_{char}}. \quad (49)$$

308 This mass flow rate represents the amount of oxygen per unit time that is required in the air
 309 reactor to return the oxygen carrier to its original oxidization state. The mass flow rate to be
 310 added at the fuel reactor injection to reproduce biomass conversion and reduction reactions is
 311 $\dot{Q}_{CO_2} + \dot{Q}_{H_2O}$.

Table 3: Inlet mass flow rates: experiments and simulation with lateral injection of products.

| Item | Simulation | | Experiments | |
|-----------------------------------|-------------|-----------------------------------|-------------|----------------|
| AR primary gas inlet | 124.49 kg/h | N ₂ ,O ₂ | 146.67 kg/h | Air |
| AR secondary gas inlet G1 | 14.46 kg/h | N ₂ ,O ₂ | 17.04 kg/h | Air |
| AR secondary gas inlet G2 | 24.75 kg/h | N ₂ ,O ₂ | 29.16 kg/h | Air |
| FR bottom inlet | 11.66 kg/h | N ₂ | 11.66 kg/h | N ₂ |
| FR lateral inlet | 49.27 kg/h | CO ₂ ,H ₂ O | 20.2 kg/h | Bio |
| Lifter inlet | 2.27 kg/h | N ₂ | 2.27 kg/h | N ₂ |
| AR loop seal, particle inlet leg | 2.23 kg/h | N ₂ | 2.23 kg/h | N ₂ |
| AR loop seal, particle outlet leg | 3.21 kg/h | N ₂ | 3.21 kg/h | N ₂ |
| FR loop seal, particle inlet leg | 2.15 kg/h | N ₂ | 2.15 kg/h | N ₂ |
| FR loop seal, particle outlet leg | 1.73 kg/h | N ₂ | 1.73 kg/h | N ₂ |

312 Three ways of injecting such additional gases to mimic reactions are tested:

- 313 • Lateral injection of products: the CO₂-H₂O mixture, corresponding to the whole products
 314 from the full biomass conversion and reduction reactions (therefore accounting for the
 315 oxygen from ilmenite), is injected in the fuel reactor from the lateral inlet, which is at the
 316 same location as the fuel particle inlet, according to the experimental configuration; the
 317 oxygen consumed by the oxidation is directly removed from the AR inlet. In this case, the
 318 primary and secondary inlets to AR are reduced with 15% compared to the experimental
 319 values.
- 320 • Bottom injection of products: the CO₂-H₂O mixture is injected in the fuel reactor from
 321 the bottom inlet, together with the fluidizing gas (N₂); the inlet conditions in the AR are
 322 the same as above.
- 323 • Lateral injection of a part of the products while using source terms for the oxygen transfer:
 324 inlet conditions for the air reactor are kept the same as in the experiments. The change
 325 of flow rate due to the mass transfer between the oxygen carrier and the gas phase is
 326 taken into consideration by source terms for both the air and fuel reactors. This method
 327 of injection allows part of the gases to be distributed inside the reactors in proportion to

328 the local amount of solid. In the fuel reactor, the source terms for CO₂ and H₂O in each
 329 computational cell are computed as follows:

$$\Gamma_{CO_2}^{FR}(\mathbf{x}, t) = \dot{Q}_{O_2} Y_{CO_2}^* \frac{\alpha_{oc}(\mathbf{x}, t) \rho_{oc}(\mathbf{x}, t)}{m_{oc,FR}(t)}, \quad \Gamma_{H_2O}^{FR} = \dot{Q}_{O_2} Y_{H_2O}^* \frac{\alpha_{oc}(\mathbf{x}, t) \rho_{oc}(\mathbf{x}, t)}{m_{oc,FR}(t)}, \quad (50)$$

330 where $Y_{CO_2}^*$ and $Y_{H_2O}^*$ are the mass fractions of CO₂ and H₂O in the FR products, accord-
 331 ing to a full conversion assumption (i.e. $Y_{CO_2}^* + Y_{H_2O}^* = 1.0$). $\alpha_{oc}(\mathbf{x}, t)$ and $\rho_{oc}(\mathbf{x}, t)$ are,
 332 respectively, the particle volume fraction and density in the corresponding computational
 333 cell. $m_{oc,FR}(t)$ is the instantaneous total solid mass in the fuel reactor.

334 For the air reactor, the source term is written as

$$\Gamma_{O_2}^{AR} = -\dot{Q}_{O_2} \frac{\alpha_{oc}(\mathbf{x}, t) \rho_{oc}(\mathbf{x}, t)}{m_{oc,AR}(t)},$$

336 where $m_{oc,AR}(t)$ is the instantaneous total mass of oxygen carrier in the air reactor. This
 337 term is negative because of the oxidation reaction, which leads to a mass transfer of
 338 oxygen from the gas to the solid phase.

339 The evaluation of the injection methods will be shown in section 4.1.

340 The gas and solid flow rates from experiments are given in Table 3, as well as the gas flow
 341 rates considered in the numerical simulation according to the lateral injection method (the first
 342 presented above). Loop-seal and lifter injection rates correspond to the experimental operating
 343 conditions, except for the injection temperature (here set to 1273 K).

344 4. Results and discussion

345 Hereafter, if not otherwise mentioned, results refer to the uncorrelated model case (cf.
 346 Equation (44)), with a free-slip mean particle velocity wall boundary condition. Results indicate
 347 that the system reaches a hydrodynamic steady state from about 15 seconds. Accordingly, to
 348 get statistics from the numerical simulations (pressure, velocity, solid mass flow rate, etc.),
 349 time-averaging of the results starts after 15 seconds of physical time.

350 4.1. Injection method

351 First, the three different methods of injection are tested to assess their effect on the numerical
 352 predictions. Time-averaged pressure profiles obtained by the numerical simulations are shown
 353 in Figure 3. In the figure, experimental pressure measurements are also shown. The given
 354 pressures are gauge pressures, with the atmosphere as the zero reference. The numerical results
 355 are almost identical to each other in the air reactor, as well as in the lifter. In the fuel reactor,
 356 however, the bed expansion is slightly higher between 0.5 and 3 meters when injecting from the
 357 bottom or when using local source terms to account for oxygen mass transfer. The results are
 358 consistent with each other, though. Indeed, injecting from the bottom, or directly introducing
 359 the gas in the reactor by source terms, should lead to a more homogeneous bed for which
 360 a larger expansion is expected. This is more pronounced when introducing the gas in each
 361 computational cell.

362 Globally, results indicate that the air reactor operates in a circulating regime, with a denser
 363 part at the bottom, as expected. In contrast, the pressure profiles in the fuel reactor exhibit
 364 two smoothly connected linear trends, typical of bubbling fluidized beds. The slope of the
 365 pressure in the upper part of the fuel reactor indicates however that a part of the solid leaves

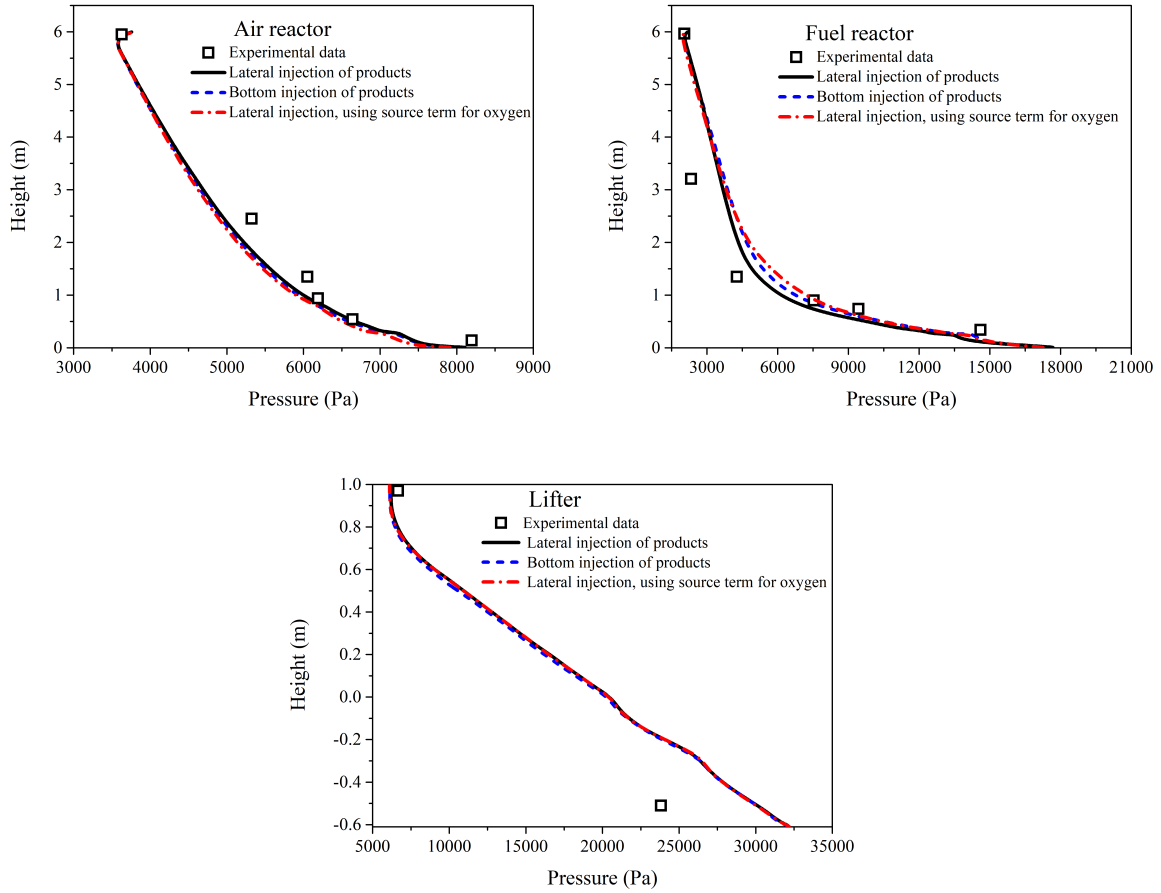


Figure 3: Time-averaged pressure using three different injection methods.

366 the reactor at the top. The fuel reactor operates therefore in a mixed regime, as observed in
 367 the experiments.

368 From now on, the lateral injection will be used for the numerical simulations. This injection
 369 method along with the uncorrelated model and the free-slip boundary condition represent our
 370 reference case. In the reference case, the particle density is set to 4727 kg/m^3 (as already
 371 mentioned). The question of the particle density is discussed in Section 4.4.

372 4.2. Flow pattern

373 Instantaneous concentrations of the particulate phase (oxygen carrier) are computed and
 374 displayed in Figures 4 and 5, at different times, to provide information of the flow evolution in
 375 the system. In the air reactor, particles are fluidized and carried by the fluidization gas, then
 376 they are separated by the cyclone and fall down into the loop seal. After passing the loop seal,
 377 particles then enter the fuel reactor. The lifter is located between the air reactor and the fuel
 378 reactor and works as an additional connector for transporting particles from the fuel reactor to
 379 the air reactor. As can be seen, there are bubbles between the fuel reactor and the lifter. In a
 380 real reactive case, attention should be paid to the flow rate of fuel particles entering the lifter
 381 from the fuel reactor, which could dramatically affect the carbon capture efficiency, since such
 382 particles will be transported to the air reactor where they will burn, producing CO_2 . Results
 383 show that the solid volume fraction is higher in the fuel reactor than in the air reactor because
 384 of the different gas velocity. The evolution in time of the solid volume fraction within the fuel
 385 reactor is shown in Figure A.23, on a plane located in the middle of the reactor. To get a better

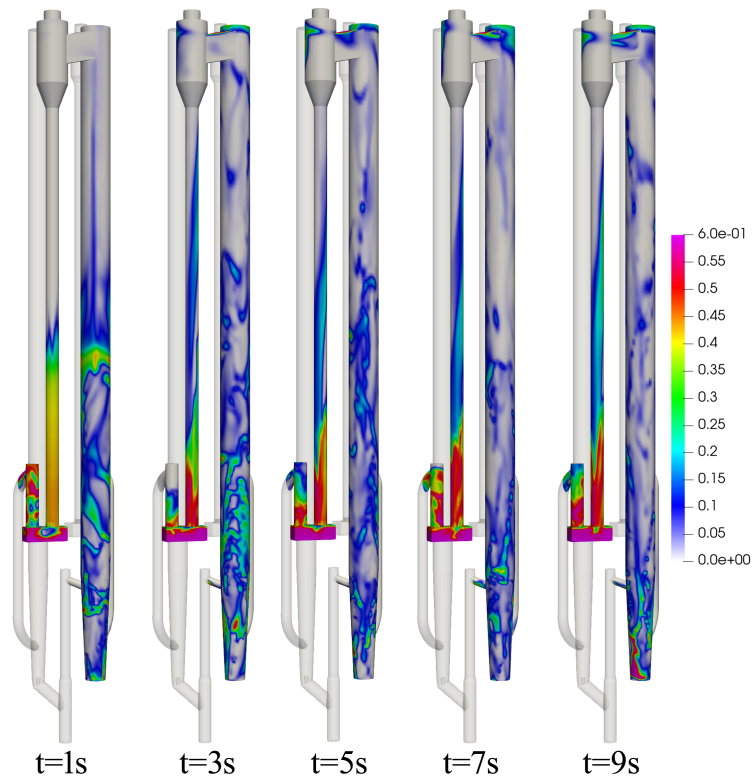


Figure 4: Instantaneous solid volume fraction: air reactor view.

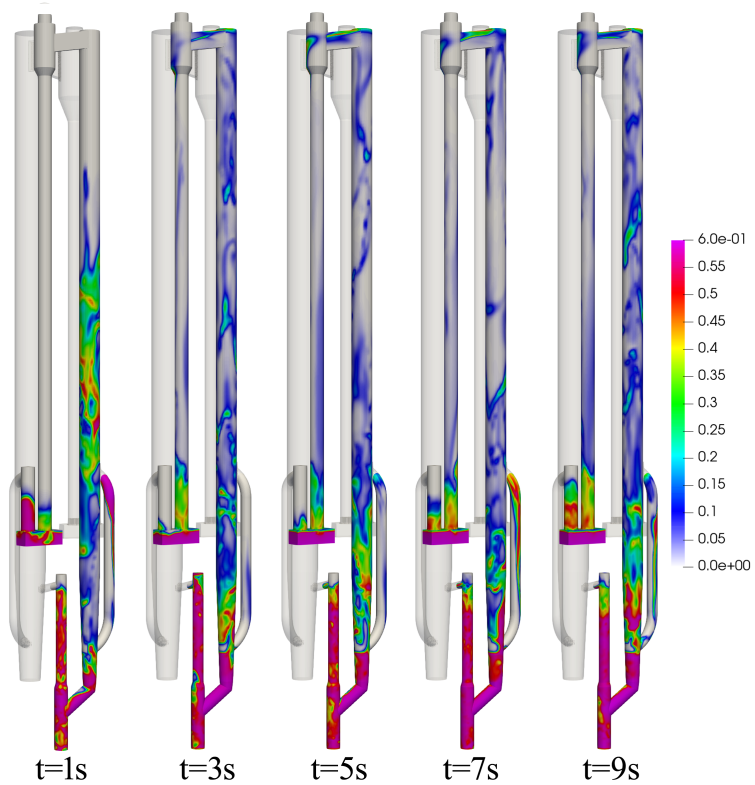


Figure 5: Instantaneous solid volume fraction: fuel reactor and lifter view.

386 look, the view is zoomed from 0 to 3 meters in height. The bubble formation, breakage and
 387 the flow state can be observed.

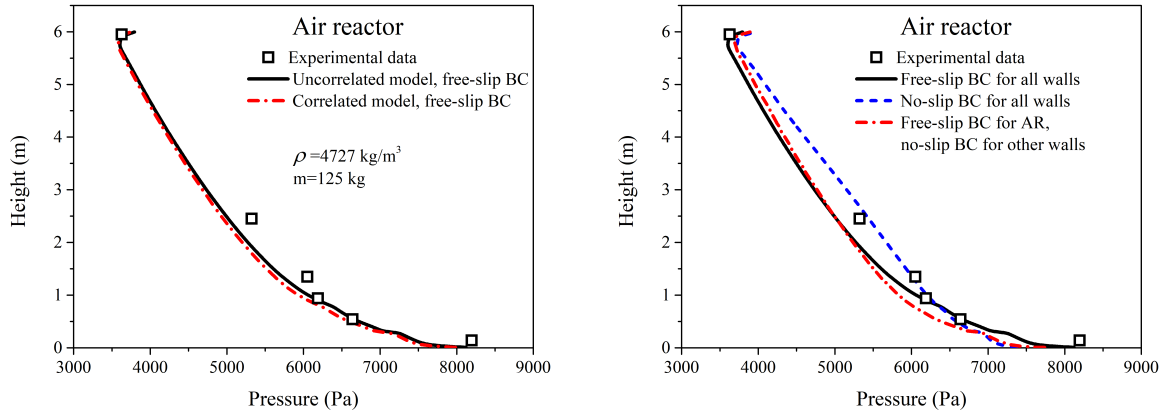


Figure 6: Time-averaged pressure in the air reactor. Comparison between collision models (left) and between mean particle velocity boundary conditions while using the same uncorrelated model (right).

4.3. Collision model and mean particle velocity wall boundary condition

In this section, the effects of the collision model and the mean particle wall velocity boundary condition on the numerical predictions are analyzed. To properly read the results that will follow, it is important to keep in mind that, in the numerical simulations, the pressure at the outlet was estimated from the experimental pressure in each reactor at the same height, subtracting the pressure between the reactor and its corresponding cyclone. Such an estimate was computed using the free-slip boundary condition, and the corresponding value set as an outlet condition for all the numerical simulations, including those that use the no-slip boundary condition. For the latter, a shift in the pressure profile with respect to the experimental measurement is therefore expected. This point does not deserve further analysis since it is due solely to the pressure outlet conditions.

Figure 6 compares numerical results and experimental measurements of the time-averaged pressure in the air reactor. In Figure 6 (left) both the uncorrelated and correlated model results are shown, using the same free-slip boundary condition. The results reveal only little difference between the two numerical model predictions in the air reactor. The pressure profiles in the fuel reactor and lifter are shown in Figure 7 (top). No appreciable difference is found between the uncorrelated and correlated model predictions in these zones.

The solid mass corresponding to each element of the CLC system is calculated by a volume integral using the time-averaged solid volume fraction, together with the constant particle density. Results are listed in Table 4. Comparison between correlated and uncorrelated models confirms very few differences in the solid mass distribution as well. They are slightly more pronounced in the air reactor, where the particulate phase is more dilute and the effects of a correlated contribution to the particle velocity fluctuation, due to the interactions with the fluid, should be more important than in the fuel reactor and lifter. This point will be discussed further in Section 4.6.

The effect of the mean particle velocity boundary condition on the numerical predictions is then analyzed. No-slip and free-slip wall boundary conditions correspond to the limit cases of maximum particle wall friction effect and pure elastic frictionless particle bouncing, respectively. The results indicate that the wall boundary conditions significantly affect the solid flow behavior. As shown by Figure 6 (right), the pressure obtained using the no-slip wall boundary condition corresponds to an increase of the solid entrainment in the air reactor. To exclude any substantial dependency on the coupling of the different parts of the system, an additional

Table 4: Solid mass distribution using different collision models and mean particle velocity wall boundary conditions (units: kg).

| | CASE 1 uncorrelated free-slip | CASE 2 correlated free-slip | CASE 3 uncorrelated no-slip |
|--------------------------|-------------------------------------|-----------------------------------|-----------------------------------|
| Air reactor | 15.656 | 15.194 | 12.662 |
| Fuel reactor | 24.597 | 24.889 | 26.768 |
| Lifter | 19.698 | 19.832 | 18.895 |
| AR loop seal and cyclone | 34.277 | 34.308 | 35.908 |
| FR loop seal and cyclone | 30.771 | 30.777 | 30.707 |
| Total mass | 125.00 | 125.00 | 125.00 |

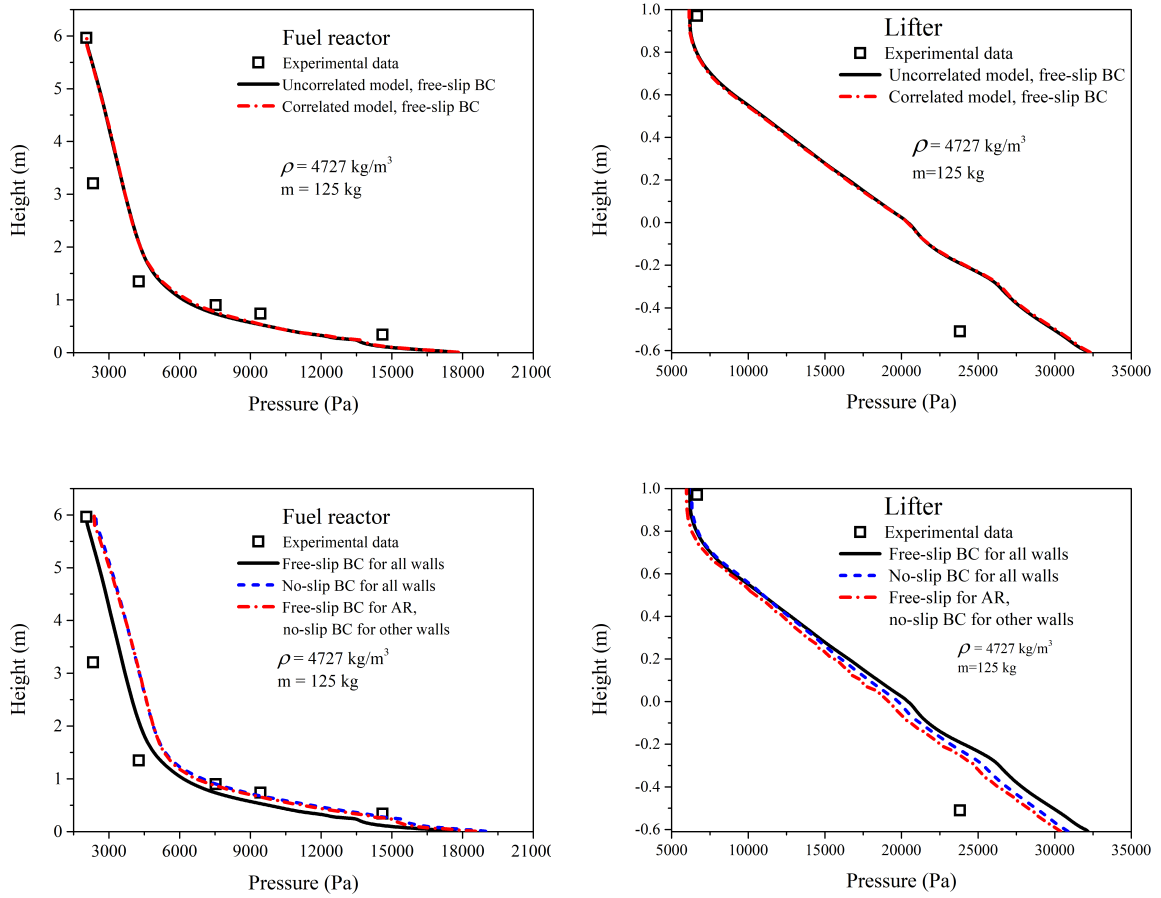


Figure 7: Time-averaged pressure in the fuel reactor and lifter. Comparison between collision models (top), and between mean particle velocity boundary conditions while using the same uncorrelated model (bottom).

420 simulation was carried out. Starting from the end (i.e. 40 seconds of physical time) of the
 421 simulation that uses uncorrelated model and no-slip boundary condition everywhere, the free-
 422 slip boundary condition was applied to the air reactor only. This simulation was run for an
 423 additional 45 seconds, and averages in time were computed from 65 to 85 seconds. The results
 424 (Figure 6 (right)) show that the pressure profile mostly returns to the one obtained when the
 425 free-slip boundary condition was used everywhere in the system. This demonstrates that the

426 changes in pressure predictions are mainly due to the flow behavior within the air reactor rather
 427 than on the coupling of the entire system. We can conclude that the no-slip condition in the AR
 428 is the reason for a larger extension of the linear pressure gradient, corresponding to a reduced
 429 acceleration region of the solid phases, which leads to a more efficient entrainment by the gas
 430 flow.

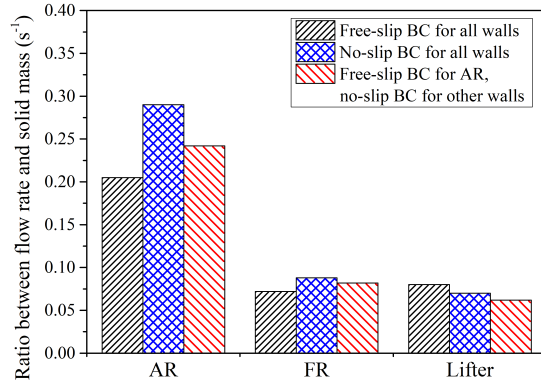


Figure 8: Effect of the mean particle velocity boundary condition on the entrainment estimated as the ratio between the solid mass flow rate and the solid mass.

431 Only smaller differences are observed when comparing free-slip and no-slip boundary condi-
 432 tion results in the fuel reactor and lifter (Figure 7 (bottom)). The no-slip boundary condi-
 433 tion leads to slightly higher expansion of the denser part of the bed in the fuel reactor (roughly
 434 estimated as the point of intersection of the tangents corresponding to the two linear pressure
 435 distributions in the pressure profiles). This observation is consistent with the results of the work
 436 of [Fede et al. \(2016\)](#) who showed that a no-slip boundary condition acts at reducing the down-
 437 ward solid mass flux at the walls in a dense fluidized bed, leading to a more expanded bed. The
 438 no-slip boundary condition also affects the slope of the pressure profile in the lifter. However,
 439 Figure 7 (bottom right) shows that, for the lifter, the effect of the coupling is more important
 440 than the boundary condition itself. Globally, in the fuel reactor, the agreement between the
 441 numerical results and experimental data is good, except in the penultimate measurement point,
 442 while an overestimation of the pressure is observed at the bottom of the lifter.

443 In contrast to what is observed when comparing the two collision models, the mass distri-
 444 bution changes considerably with the boundary condition (see Table 4). In particular, the
 445 mass increases in the fuel reactor and decreases in the air reactor when the no-slip boundary
 446 condition is used. In order to estimate the effect of the boundary conditions on the entrain-
 447 ment, which is strictly related to the mass distribution, the ratio between the solid mass flow
 448 rate and the solid mass in each relevant part of the system is computed. [Molodtsov \(2003\)](#)
 449 (and references cited in) showed indeed that a fully developed gas-particle flow in dilute regime
 450 (typical of circulating fluidized beds) exhibits a linear dependency of the solid flux on the solid
 451 concentration at a given superficial gas velocity, according to the regime. Since the gas flow
 452 rate in the air reactor is almost the same, regardless of the boundary condition, the solid mass
 453 flow rate and solid mass are expected to be linearly related, at the operating conditions consid-
 454 ered here. Therefore, also their ratio should be almost the same if the boundary condition had
 455 no effect on the numerical predictions. Figure 8 shows instead that this ratio increases with
 456 the no-slip boundary condition in the air reactor, confirming the conclusions drawn from the
 457 pressure profiles.

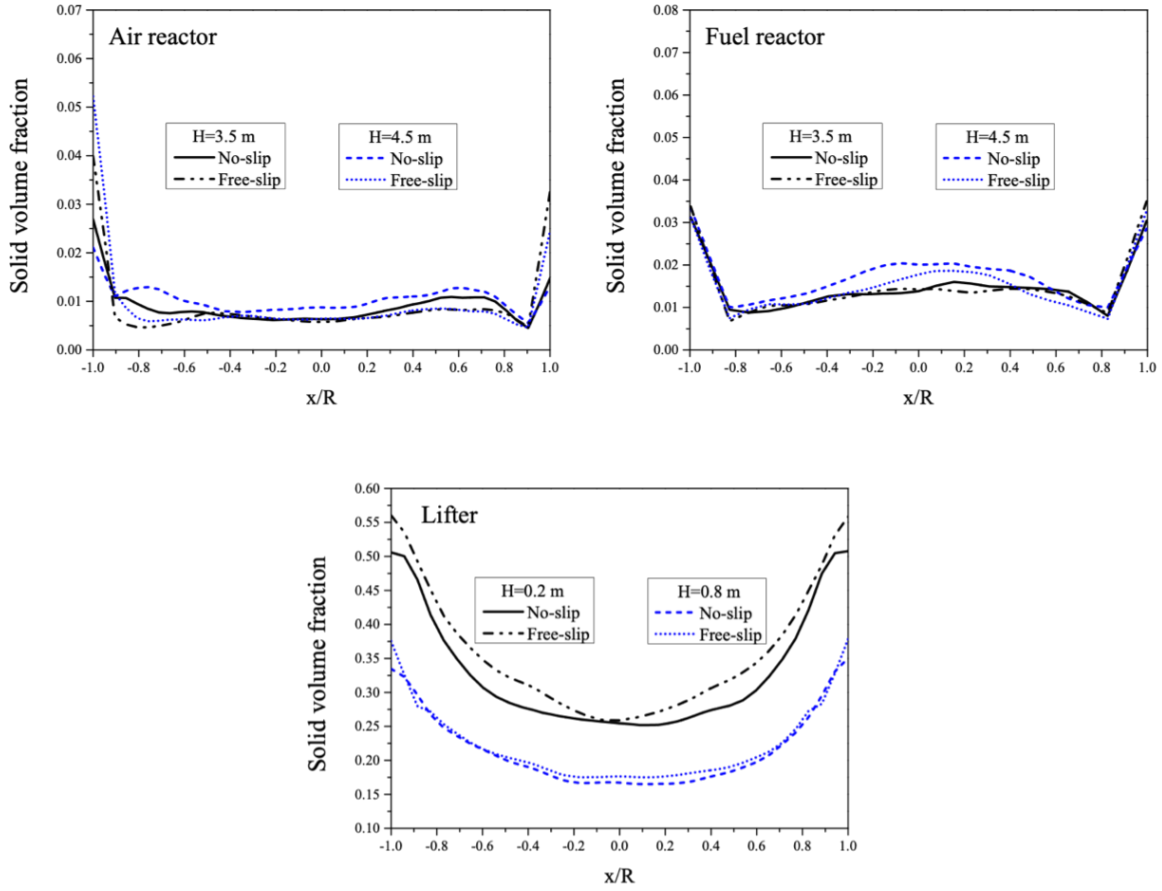


Figure 9: Radial profiles of the time-averaged solid volume fraction in air reactor, fuel reactor and lifter at different heights, depending on the mean particle velocity boundary condition.

458 The radial profiles of the time-averaged solid volume fraction in the system are shown in
 459 Figure 9. No significant effect of the boundary condition is observed in the fuel reactor and
 460 lifter, away from the injections. In contrast, results indicate that in the air reactor the no-slip
 461 boundary condition leads to lower values of the solid volume fraction at the wall than the
 462 free-slip condition. A possible explanation is the additional production of the particle fluctuant
 463 kinetic energy, q_s^2 , due to the larger values of the particle velocity gradient imposed at the wall
 464 by the no-slip condition. As a matter of fact, such larger values of q_s^2 close to the wall lead
 465 to a “turbophoresis” effect that pushes the particles back towards the core of the flow. The
 466 time-averaged particle fluctuant kinetic energy is displayed in Figure 10 on a selected plane in
 467 the center of the system.

468 The radial profiles of the time-averaged solid vertical velocity are shown in Figure 11. In the
 469 fuel reactor, as expected, particles flow up in the center and down near the wall. Negative solid
 470 velocities are found in the air reactor as well, also at the top. For the lifter, the trend is similar,
 471 while the values are lower. The effect of the mean particle velocity wall boundary condition
 472 on the particle velocity is not really conclusive. Radial profiles are not symmetric in the air
 473 reactor, and it is unclear whether this asymmetry depends on the convergence of the numerical
 474 simulation or on the influence of the injections, even at these heights. We can however observe
 475 a decrease of the solid axial velocity in the air reactor when a no-slip condition is used at these
 476 two heights.

477 In conclusion, results suggest that while a no-slip condition can be considered satisfactory

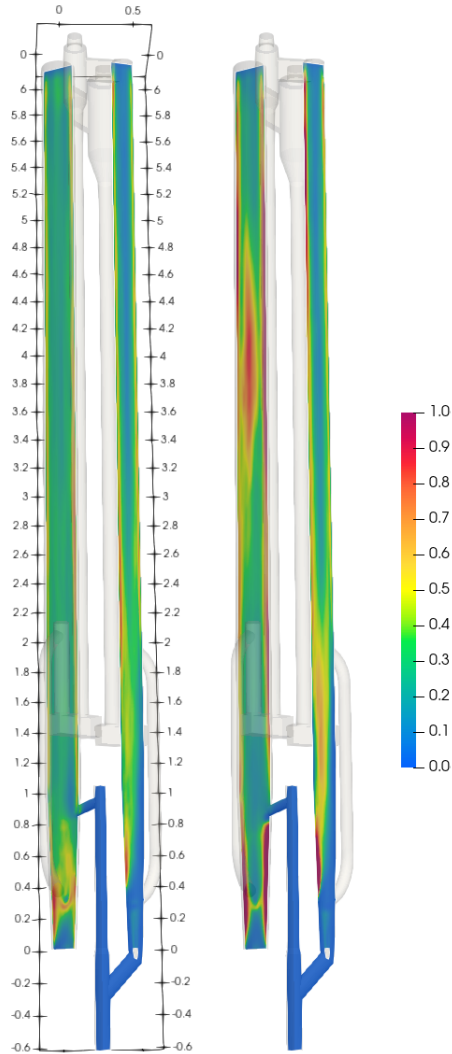


Figure 10: Time-averaged particle fluctuant kinetic energy, q_s^2 , on a plane in the middle of the system using free-slip (left) and no-slip (right) mean particle velocity wall boundary conditions.

478 in a dense regime (fuel reactor, lifter), its use is very questionable in dilute zones (air reactor).

479 4.4. Particle density and solid mass inventory

480 The bulk density of the oxygen carrier is given by the experiments and has a value of 2600
 481 kg/m³. To recover the value of the particle density (needed for the numerical simulations) one
 482 must know the mean packed-bed voidage, which depends on several parameters including the
 483 particle shape. Results presented so far were obtained with a particle density of 4727 kg/m³,
 484 corresponding to a mean voidage of 0.45. This value is consistent with the specific gravity
 485 of ilmenite found in the literature. However, the oxygen carrier is not pure ilmenite and its
 486 composition also changes with redox cycles. [Abad et al. \(2011\)](#) reported a lower true density
 487 for the ilmenite oxygen carrier, also depending on the particle state (pre-oxidized or activated),
 488 and an increasing porosity of the most oxidized state with particle activation. Since the exact
 489 value to be attributed to a spherical particle modeling the real material (including pores) is
 490 a priori unknown, additional numerical simulations were carried out using a lower density to
 491 investigate the influence of the particle density on the numerical predictions. A particle density
 492 corresponding to the maximum packing (0.64) was considered, i.e. 4062 kg/m³. The numerical
 493 predictions of the pressure using the two different particle densities are shown in [Figure 12](#).

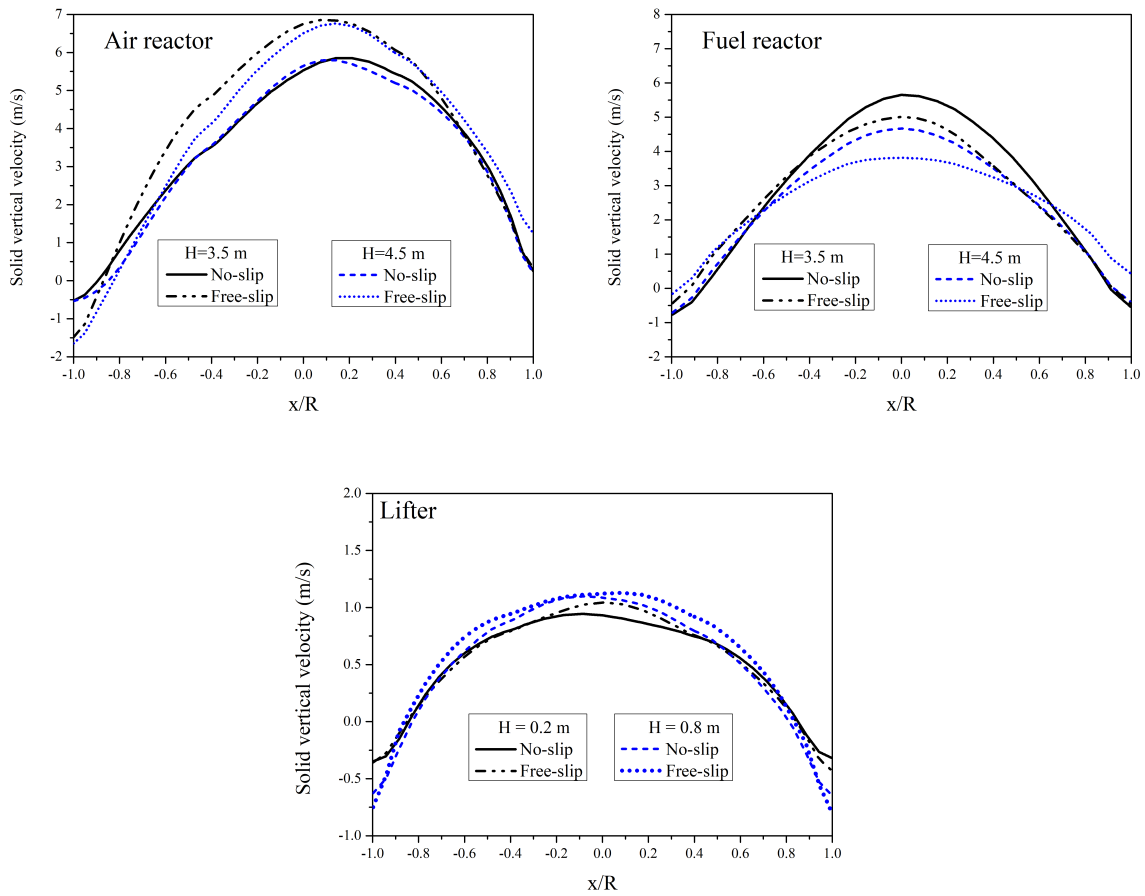


Figure 11: Radial profiles of the time-averaged solid vertical velocity in air reactor, fuel reactor and lifter at different heights, depending on the mean particle velocity boundary condition.

494 The corresponding integrated mass distribution is given in Table 5. The results show that the
 495 pressure is overestimated by the lowest particle density in the air reactor. Globally, the mass
 496 in the air reactor is higher, and comes mainly from the loop seals and lifter (see Table 5). In
 497 the fuel reactor, the pressure is also overestimated by the lowest particle density with respect
 498 to the highest density. A greater difference is observed in the lifter where the density makes
 499 the slope of the pressure to change. The pressure is better predicted at the bottom than at the
 500 top in this case (because of the coupling effect).

501 In order to investigate the effect of the mass inventory, an additional numerical simulation
 502 was carried out. In this simulation the mass was decreased in order to improve the numerical
 503 predictions obtained with the lowest density. Comparing the two cases with the same particle
 504 density and different mass inventory, it turns out that the smaller the mass, the smaller the
 505 pressure at the bottom of the air reactor, as well as in the fuel reactor, as expected. Further,
 506 the results show that decreasing the mass inventory gives a better agreement with the experimen-
 507 tal data in the lifter, but not in the other reactors. Noteworthy is that the total solid inventory
 508 does not change the slope of the pressure profile in the lifter, since this connection operates
 509 almost filled with particles, in a very dense regime, and therefore its total mass is primarily
 510 determined by the particle density.

511 4.5. Mesh refinement (sub-grid scale effects)

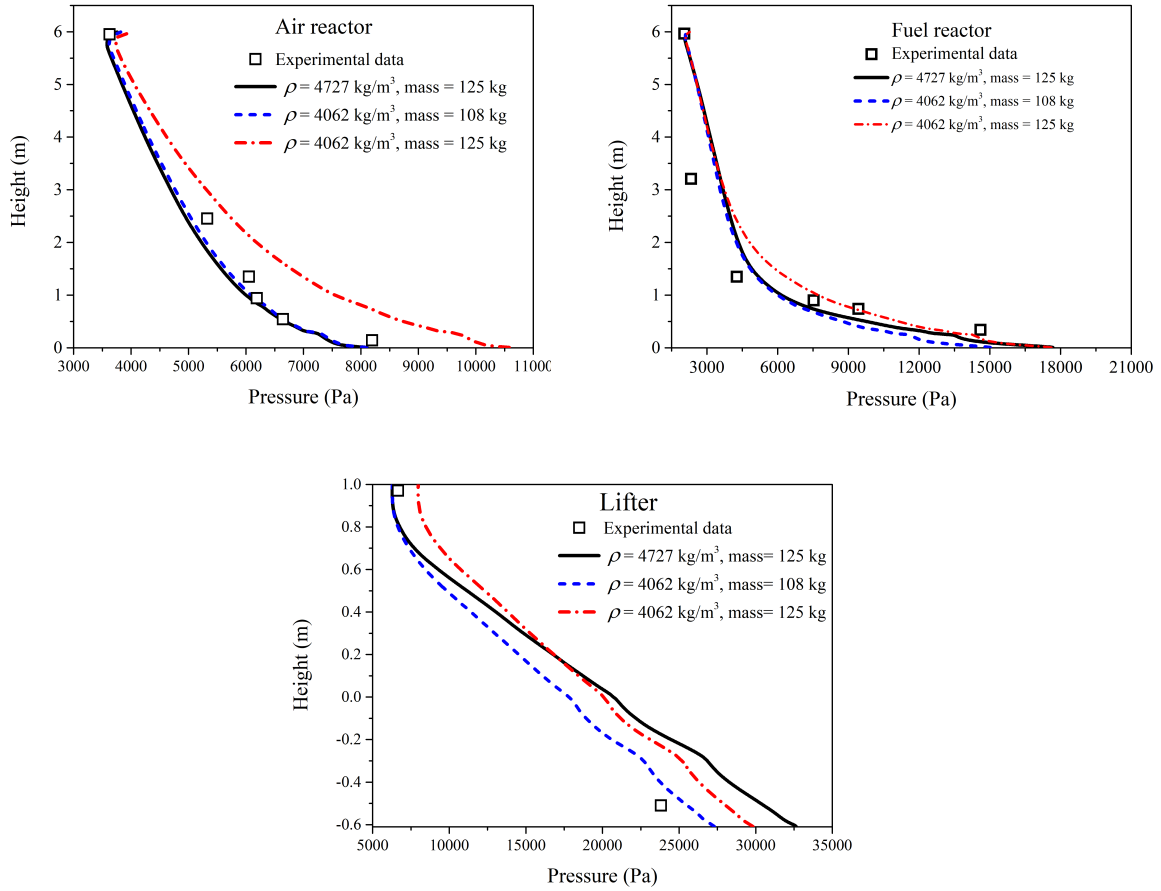


Figure 12: Time-averaged pressure depending on the particle density and solid inventory.

512 Drag modeling is a crucial aspect of the closure assumptions for the accurate prediction of
513 fluidized beds using the Euler-Euler simulation approach. The main issue is the ability of the
514 numerical simulation to take into account solids segregation effects, such as the formation of
515 clusters in circulating fluidized beds, which can occur at very small length scales but with a
516 very strong effect on the macroscopic hydrodynamics, in particular on the entrainment of the
517 solid by the gas flow. Thus, the question of the drag closure model is directly related to the
518 refinement of the mesh towards the characteristic length scale typical of the clustering effect.
519 As pointed out by [Igci and Sundaresan \(2011b\)](#) and [Ozel et al. \(2013\)](#), if the mesh is not
520 sufficiently refined, the Euler-Euler equations of momentum and random kinetic energy have to
521 be supplemented by additional terms accounting for the clustering of particles at the sub-grid
522 scale. The dominant effect is the overestimation of the drag term, which can be corrected
523 using different approaches such as the energy minimization multi-scale (EMMS) approach ([Li
524 and Kwauk \(1994\)](#)), or the sub-grid scale drift velocity modeling ([Igci and Sundaresan \(2011a\);
525 Parmentier et al. \(2012\); Ozel et al. \(2013\)](#)). While previous studies have shown that the effect
526 of the sub-grid drag modeling depends on the mesh size and particle characteristics (see, e.g.,
527 [Wang et al. \(2009\)](#)), unfortunately there are still no universal dimensionless parameters that
528 allow an a priori assessment of sub-grid scale effects and the need to consider sub-grid drag
529 closures. However, it is found that the sub-grid scale effect decreases with the particle inertia
530 and is much less effective for Geldart-B particles, such as those considered in the present study.

531 In order to estimate the unresolved clustering effect, which is expected to lead to an overesti-

Table 5: Solid mass in the system with different density and/or total inventories (units: kg).

| | CASE 1 $\rho_p = 4727 \text{ kg/m}^3$ $m_{total}=125 \text{ kg}$ | CASE 4 $\rho_p = 4062 \text{ kg/m}^3$ $m_{total}=125 \text{ kg}$ | CASE 5 $\rho_p = 4062 \text{ kg/m}^3$ $m_{total}=108 \text{ kg}$ |
|--------------------------|------------------------------------------------------------------------|------------------------------------------------------------------------|------------------------------------------------------------------------|
| Air reactor | 15.656 | 23.787 | 15.257 |
| Fuel reactor | 24.597 | 25.217 | 20.739 |
| Lifter | 19.698 | 16.596 | 16.072 |
| AR loop seal and cyclone | 34.277 | 31.329 | 28.885 |
| FR loop seal and cyclone | 30.771 | 28.071 | 27.047 |
| Total mass | 125.00 | 125.00 | 108.00 |

Table 6: Solid mass in the system depending on the mesh refinement (units: kg).

| | CASE 1 Reference mesh | CASE 6 Refined mesh |
|--------------------------|--------------------------|------------------------|
| Air reactor | 15.656 | 16.508 |
| Fuel reactor | 24.597 | 25.564 |
| Lifter | 19.698 | 19.798 |
| AR loop seal and cyclone | 34.277 | 33.323 |
| FR loop seal and cyclone | 30.771 | 29.807 |
| Total mass | 125.00 | 125.00 |

532 mation of the solid entrainment, and to assess the need for a sub-grid drag model, an additional
533 numerical study with a refined mesh was carried out. The numerical simulation was performed
534 by decreasing the mesh size in each direction by a factor of two, in both the air reactor and
535 fuel reactor.

536 Figure 13 compares the time-averaged pressure predictions obtained using the reference
537 mesh (716 312 cells) and the refined mesh (2 723 176 cells). The corresponding mass distribution
538 in each part of the CLC unit is provided in Table 6.

539 The results show that the effect of the refinement is low in the fuel reactor and unperceivable
540 in the lifter. Concerning the air reactor, a better agreement between numerical simulations
541 and experiments is observed when a finer mesh is used. However, the difference in pressure
542 predictions is rather small. Additionally, no substantial difference in the entrainment of the
543 solid by the gas flow is found neither in the air reactor nor in the fuel reactor (see, Figure
544 14 (left)). The mesh refinement leads to a slightly lower bed expansion in the fuel reactor, as
545 expected, but globally the solid volume fraction predictions are very close, as shown in Figure 14
546 (right). In this figure, the profiles are computed by spatially averaging the local time-averaged
547 solid volume fraction. Finally, comparing the two numerical predictions leads to the conclusions
548 that the sub-grid clustering effect is negligible for such highly inertial particles and that we can
549 overcome the use of a sub-grid drag model in our study.

550 4.6. Analysis of the CLC behavior

551 Back to the reference case (CASE 1), Figure 15 (left) shows the time evolution of the pressure
552 in the two reactors, at a selected height for each one. At these locations, the instantaneous
553 pressure is averaged in space (over a plane normal to the vertical direction). The dashed/dot-
554 dashed lines represent the mean experimental values. From about 15 seconds, numerical results

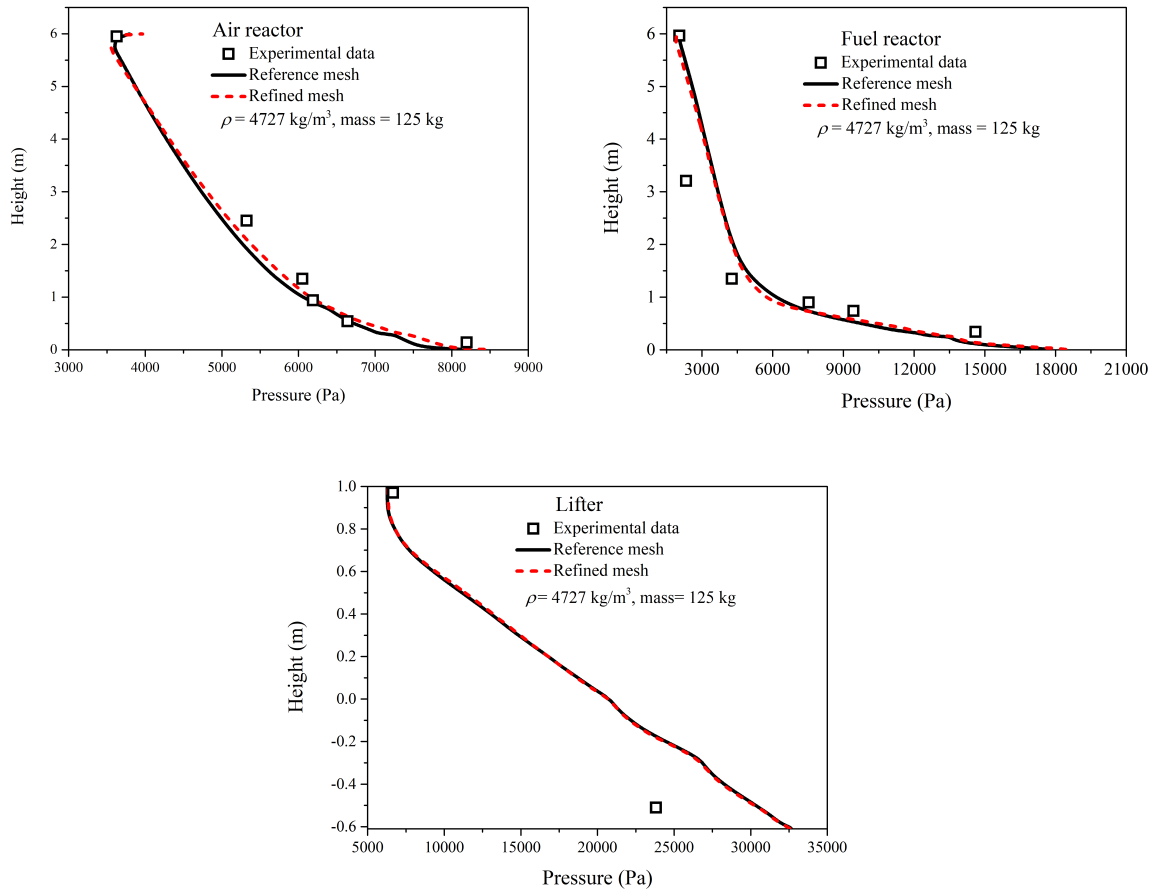


Figure 13: Time-averaged pressure depending on the mesh refinement.

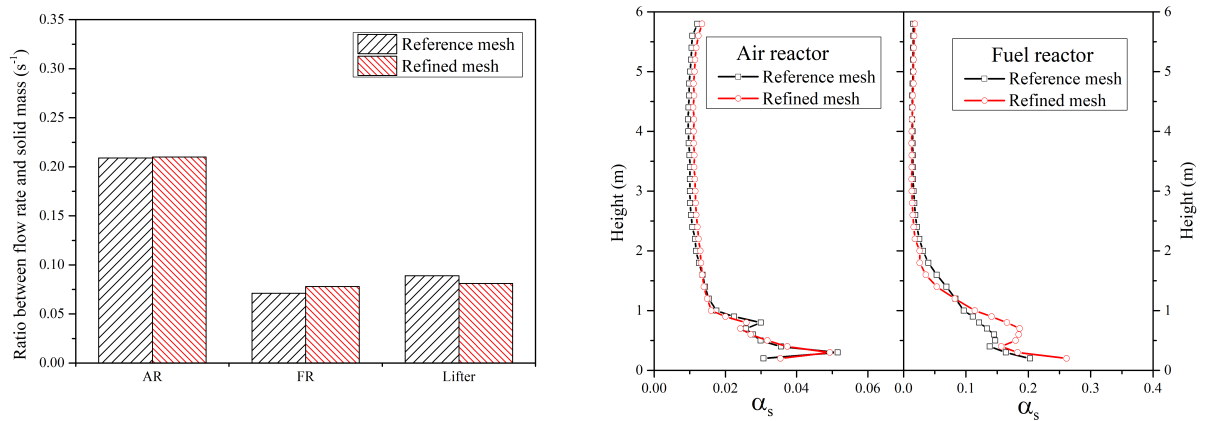


Figure 14: Effect of the mesh refinement on the entrainment (left). Time-averaged vertical profile of the solid volume fraction depending on the mesh refinement (right).

555 stabilize around a constant mean value in both the fuel and air reactors. At the selected location,
 556 the predicted pressure is very close to the experimental data in the air reactor, while it is slightly
 557 lower in the fuel reactor, which is consistent with the time-averaged profiles previously analyzed.
 558 Further, in the fuel reactor the pressure fluctuates violently around a mean value. This confirms
 559 that in this dense region, at the bottom, the fuel reactor operates rather like a bubbling fluidized

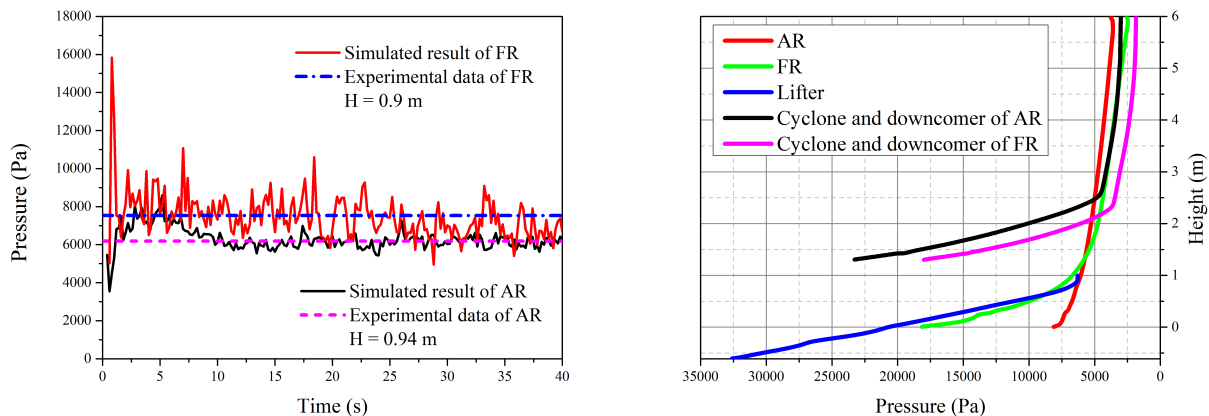


Figure 15: Time evolutions of pressure in the fuel and air reactors (left). Profiles of the time-averaged pressure in the different parts of the CLC pilot (right).

560 bed.

561 Figure 15 (right) shows the time-averaged pressure distribution along the height, according
 562 to the location in the CLC system. There is an obvious decrease of pressure with height in
 563 the lifter, and the same is true also for the fuel and air reactors. All pressure measurements
 564 depend on the amount of particle loading. The pressure balance of the current interconnected
 565 reactor system reveals that pressure is largest in the lifter and smallest in the FR cyclone. The
 566 coupling of the different unit components is clearly identified by the figure. One can recognize
 567 the connections between the bottom of the fuel reactor and the lifter, and between the top of
 568 the lifter and the air reactor, as shown in Figure 2. The pressure is the same at each connecting
 569 location. The pressure distribution therefore depends on the mass inventory in each part of
 570 the CLC unit, but also on the coupling effect of the entire system. A change in pressure that
 571 occurs in one part will lead to a pressure modification throughout the whole system.

572 The mass flow rates obtained from the numerical simulations are displayed in Figure 16
 573 (left). The mass flow rate of the solid leaving the air reactor fluctuates around a mean value,
 574 which is close to the value expected from the experiments. Results confirm that the air reactor
 575 operates as a circulating fluidized bed and that a substantial quantity of oxygen carrier leaves
 576 the air reactor from the top, according to the CLC concept and design. The fuel reactor was
 577 expected to operate in a mixed regime with most of the oxygen carriers entering the air reactor
 578 through the lifter. This regime is consistent with the profile of the mean pressure in the fuel
 579 reactor. Results show however that about half of the solid is transported from the fuel reactor
 580 to the air reactor through the lifter, while about half leaves the fuel reactor from the top and
 581 enters the air reactor through the corresponding cyclone and loop seal. This amount is higher
 582 than expected based on the design values of the experiments ($\sim 30\%$). This point will be
 583 investigated in the future, under reactive conditions.

584 In the numerical simulation, the mass of solid in each part of the system was initialized
 585 using values estimated from the pressure drop measurements in the experiments. In order to
 586 check the accuracy of such an estimation method, the time evolutions of the mass obtained
 587 from the pressure in the numerical simulation, in the two reactors, are plotted and displayed in
 588 Figure 16 (right). The time averaged results should be compared with the mean values given
 589 in Table 6 (CASE 1), computed by a volume integral using the time-averaged solid volume
 590 fraction, together with the constant particle density. The results show that the solid mass is

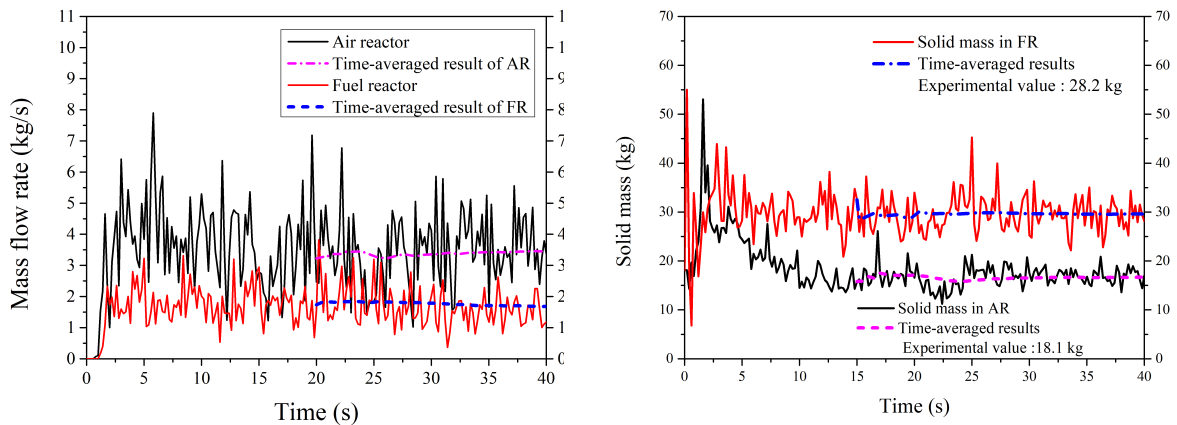


Figure 16: Time evolution of the mass flow rates of solid leaving the reactors from their top outlets (left). Time evolution of the solid mass in the air and fuel reactors (right).

591 overestimated, especially in the fuel reactor, when computed from the pressure measurements.
 592 Figure 16 (right) also shows that the solid mass in the fuel reactor stabilizes quite soon around
 593 a mean value close to the initial one. In contrast, after an initial increase, the solid mass in the
 594 air reactor decreases with time, and reaches a steady state only after 15 seconds of simulation.
 595 Further, results also show larger fluctuations in the fuel reactor compared to the air reactor,
 596 while the frequency is quite similar.

597 Figure 17 shows the time evolution of both the gas and solid velocities at a given height in
 598 the two reactors. Under the current conditions, the gas velocity is approximately 35-40% greater
 599 than the solid velocity in both the fuel and air reactors. Further, according to the numerical
 600 predictions, velocities in the air reactor are greater than in the fuel reactor, as expected. Both
 601 the gas and solid velocities fluctuate wildly due to the intense interaction between the two
 602 phases. In the experiments, the gas velocity was measured at the fuel reactor exit. A mean
 603 value is therefore available from the experiments for comparison. Figure 17 (right) shows that
 604 the numerical prediction matches well the experimental result.

605 Radial profiles of the time-averaged solid volume fraction in the two reactors and in the
 606 lifter are shown in Figure 18 at different heights. Values are plotted on a line through the
 607 center of the reactor in a radial direction. Profiles extend differently in the reactors due to the
 608 conical structure at the bottom of each. Radial coordinates are normalized by R , which is the
 609 maximum radius of the corresponding reactor. For the air reactor it corresponds to $R = 0.115$
 610 m (the radius ranges from 0.077 m (at $H = 0$ m) to 0.115 m (at $H > 1$ m)). For the fuel
 611 reactor, $R = 0.077$ m (the radius spanning from 0.05 m (at $H = 0$ m) to 0.077 m (at $H > 1$
 612 m)). For the lifter, two cylindrical zones are gradually connected by a conformal mesh. The
 613 radius of each is 0.051 m (at $-0.61 < H \leq 0$ m) and 0.039 m (at $H > 0$ m).

614 The air reactor exhibits the well-known core-annulus flow structure almost at all locations,
 615 corresponding to accumulation of particles near the wall and a more dilute regime in the center.
 616 In the air reactor, the difference between the solid volume fractions at different heights is quite
 617 small, except at the wall. Profiles are not symmetrical close to the injections. In the air
 618 reactor, the secondary gas injections are located at different heights (around $H = 0.5$ m and
 619 $H = 0.95$ m). Also the connecting parts between the air reactor and lifter ($H = 0.9$ m) affects
 620 the velocity distribution. The fuel reactor behavior is closer to that of a dense fluidized bed,
 621 but with lower solid volume fractions. The fuel reactor is indeed working in a mixed regime,

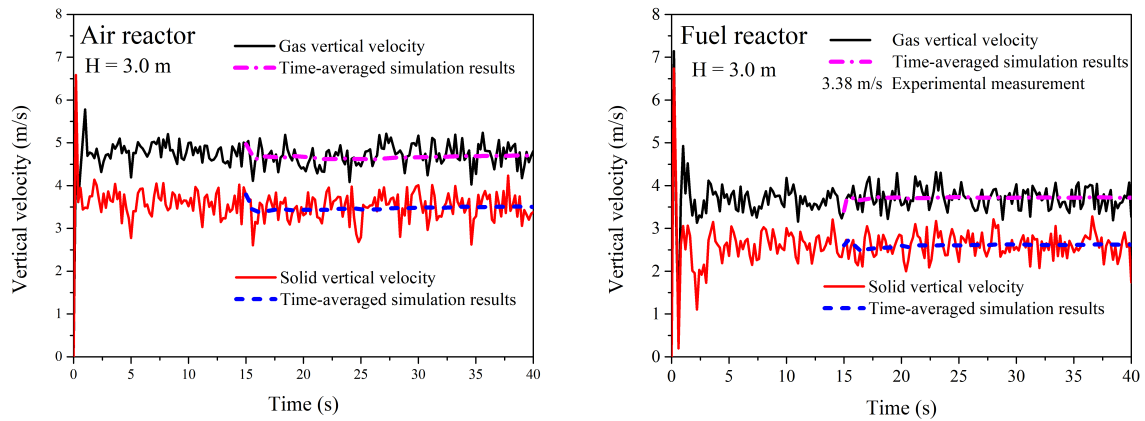


Figure 17: Time evolution of the solid and gas velocities in the air and fuel reactors.

622 bubbling and circulating, at these operating conditions. The lifter transports the particles from
 623 the fuel reactor to the air reactor by an overall upward movement, operating with high solid
 624 concentrations, especially close to the wall.

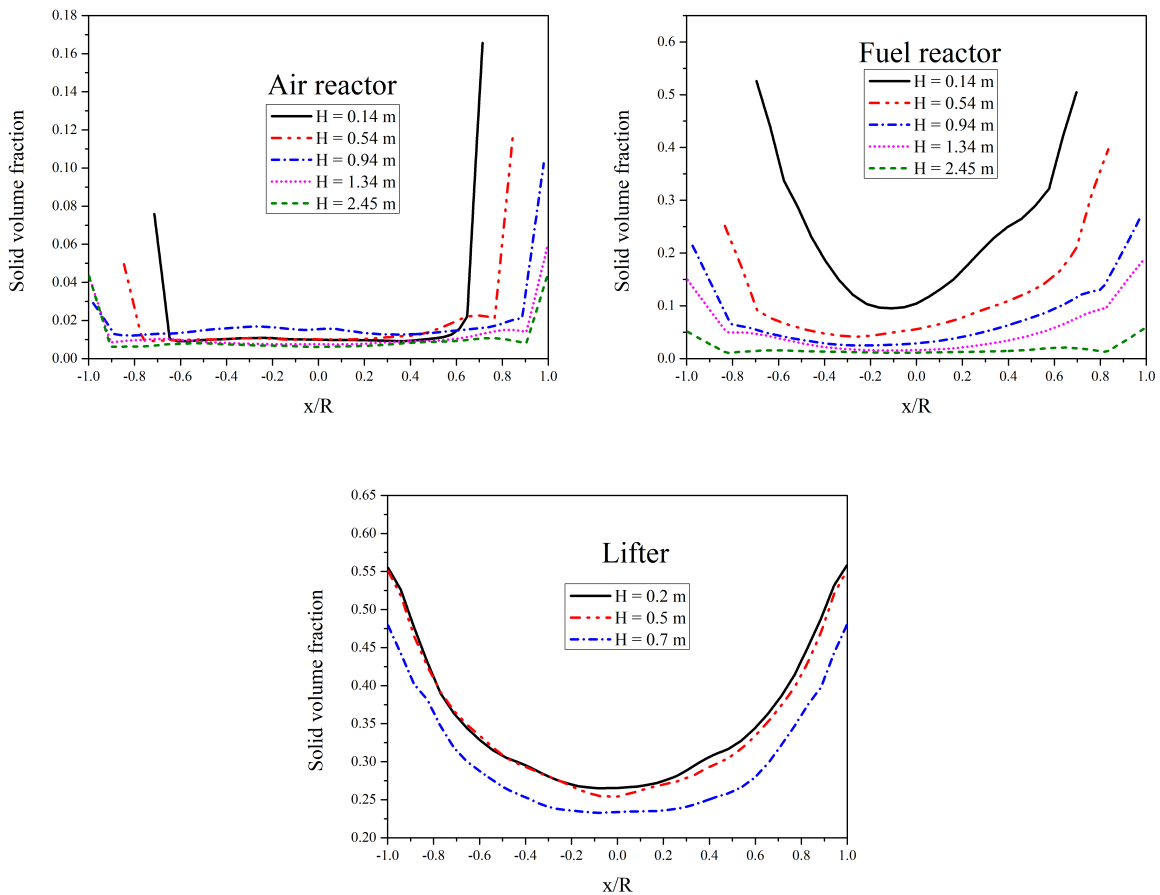


Figure 18: Radial profiles of the time-averaged solid volume fraction in the air reactor, fuel reactor and lifter, at different heights.

625 Figure 19 (top left) shows a scatterplot of the correlation coefficient used for modeling
 626 correlated and uncorrelated contributions of the particle kinetic energy in the frame of the
 627 correlated collision model. As shown in Eq. (46), such a coefficient is related to the ratio
 628 between q_{gs} and $\sqrt{4kq_s^2}$. From the figure we can observe that most of the instantaneous values
 629 are located in the range from 10^{-5} to 10^{-1} . The value of the gas-particle correlation coefficient,
 630 ζ_{gs} , is far less than 1, which leads to a very low correlation effect between neighboring particles
 631 due to their inertia with respect to the gas turbulent flow. As a result, the inter-particle collision
 632 time for correlated and uncorrelated model is nearly the same. Therefore, for the current case,
 correlated and uncorrelated models produce similar predictions.

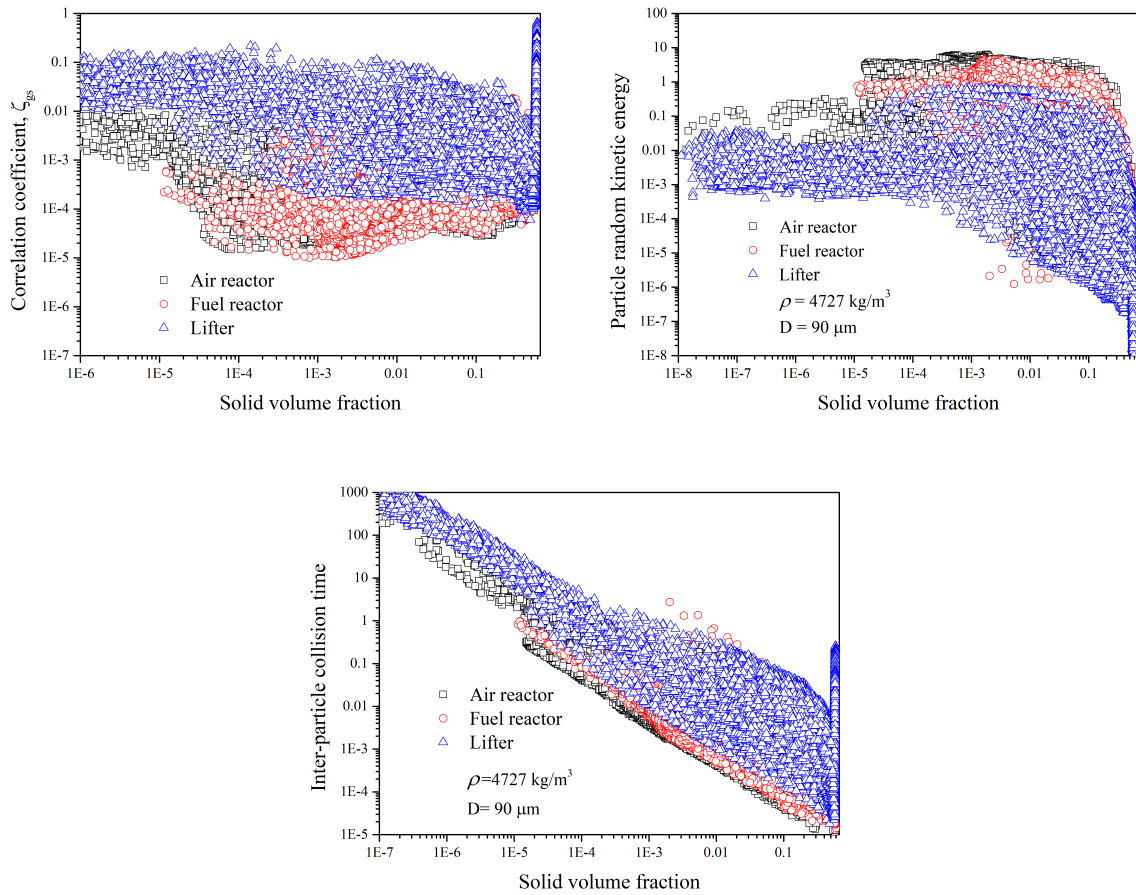


Figure 19: Instantaneous fluid-particle correlation coefficient, particle fluctuant kinetic energy and inter-particle collision time versus the solid volume fraction.

633 A scatterplot of the particle random kinetic energy versus the solid volume fraction is shown
 634 in Figure 19 (top right). Results show that in the air reactor particles are more fluctuating than
 635 in the fuel reactor, and much more than in the lifter where most of the movement is represented
 636 by a collective transport. The inter-particle collision time is shown in Figure 19 (bottom). Its
 637 dependency on the solid volume fraction is inherent to the model. Results additionally show
 638 that for a given value of the solid volume fraction, the collision time is lower in the air reactor
 639 where agitation is larger, i.e. collision frequency is higher in the part of the CLC corresponding
 640 to stronger particle fluctuations. The inter-particle collision time takes large values at the
 641 maximum compaction because the particle random kinetic energy tends to zero in such zones
 642 (see Figure 19 (top right)).
 643

644 Two additional quantities are examined, which are the ratio between the gas-particle velocity
 645 covariance, q_{gs} , and twice the gas (k) or particle (q_s^2) kinetic energies. These ratios are relevant
 646 in the interpretation of the flow behavior. Results are given in Figure 20. A first information is
 647 obtained looking at the term in Eq. (28), which represents the effect of the interphase kinetic
 648 energy exchange on the evolution of the particle random kinetic energy (Eq. (22)). Figure 20
 649 (right) shows that in all the relevant parts of the CLC the ratio $q_{gs}/2q_s^2$ is generally smaller
 650 than unity, and even smaller in the air reactor, except in very dense zones where the solid
 651 volume fraction tends to the maximum compaction. In this case q_s^2 is very small because of
 652 the larger dissipation in such zones. A ratio $q_{gs}/2q_s^2$ smaller than unity means that the term in
 653 Eq. ((28)) is a negative quantity, i.e. the particle agitation is not due to the entrainment by
 654 the turbulence, which on the contrary acts at dissipating the particle fluctuations. The same
 655 destruction effect is found in the balance equation of the gas turbulent kinetic energy (Eq.
 656 (11)), based on the interphase coupling term (Eq. (13)) and the results of Figure 20 (left).
 657 In this case, the effect of the scalar product of the drift with the relative velocity is found to
 658 be lower than the other contributions in the coupling term. More complicated is instead the
 659 interpretation of the results on the evolution of the covariance itself (Eq. (29)). Looking at
 660 the source term in Eq. (31), it comes out that the first contribution is positive. The second
 661 one depends instead on the intensity of the correlated part of the particle kinetic energy, which
 662 may be related to the ratio between the gas-particle velocity covariance and the gas kinetic
 663 energy as follow: $(q_{sg} - 2\tilde{q}_s^2) = q_{sg}(1 - q_{sg}/2k)$ (Section 2). If $q_{sg} < 2k$, a negative sign can be
 664 anticipated, which means that the second term in Eq. (31) acts at dissipating the gas-particle
 665 velocity covariance. Globally, the source term corresponding to Eq. (31) is a destruction term
 666 when $\alpha_s \rho_s / \alpha_g \rho_g > 1$.

667 Finally, Figure 21 shows snapshots of some relevant quantities of the gas-particle flow.
 668 Some of the most important information is that the gas turbulent kinetic energy is largely
 669 dissipated by the particle two-way coupling effect and is much smaller than the particle fluctuant
 670 kinetic energy. The gas turbulent viscosity is found much lower than its laminar counterpart
 671 (1.7×10^{-4} m²/s) revealing that, in the CLC at the current operating conditions, the gas
 672 turbulence predicted by the $k - \varepsilon$ model has no effect on the gas flow prediction. In addition,
 673 the correlation coefficient based on the fluid-particle velocity covariance (Eq. (46)) is very small
 674 showing that both gas and particle fluctuating velocities are uncorrelated. As a consequence, the
 675 proposed correlated model predicts that, in such a flow configuration, the random velocities of
 676 neighboring discrete particles are largely uncorrelated and the total predicted particle fluctuant
 677 kinetic energy may be recognized as the granular temperature.

678 5. Conclusion

679 A model based on the Euler-Euler approach is adopted in this study to predict the hy-
 680 drodynamic behavior of a chemical looping combustion system. Three-dimensional unsteady
 681 numerical simulations of a 150 kW_{th} pilot (operating at SINTEF, Trondheim, Norway) were
 682 carried out using NEPTUNE_CFD, with the main goal to gain insight in the local and instan-
 683 taneous flow behavior and operating characteristics. In the original experiments, the CLC pilot
 684 operated with ilmenite as oxygen carrier and biomass (wood pellet) as fuel. In this numerical
 685 study, biomass was not considered as an additional solid phase and gases from biomass conver-
 686 sion and redox reactions were accounted for by adjusting the injection conditions. Moreover, an
 687 isothermal flow was assumed, since the 150 kW_{th} CLC system operates in almost uniform tem-
 688 perature conditions, according to the experiments. The numerical geometry was built according
 689 to the experimental facility and was discretized by using a numerical mesh corresponding to a

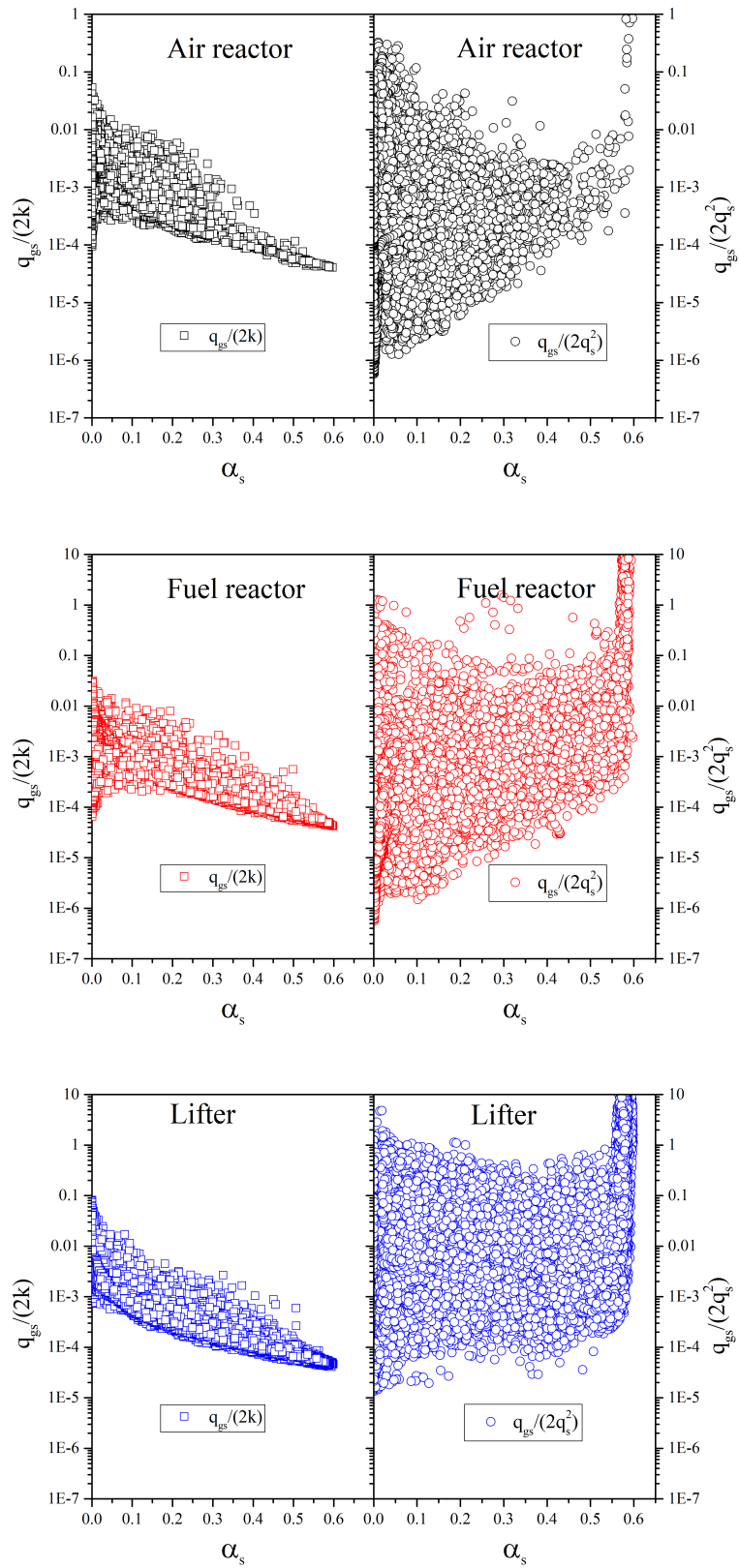


Figure 20: Instantaneous ratio between the gas-particle velocity covariance and twice the turbulent kinetic energy (on the left) or particle kinetic energy (on the right), versus the solid volume fraction.

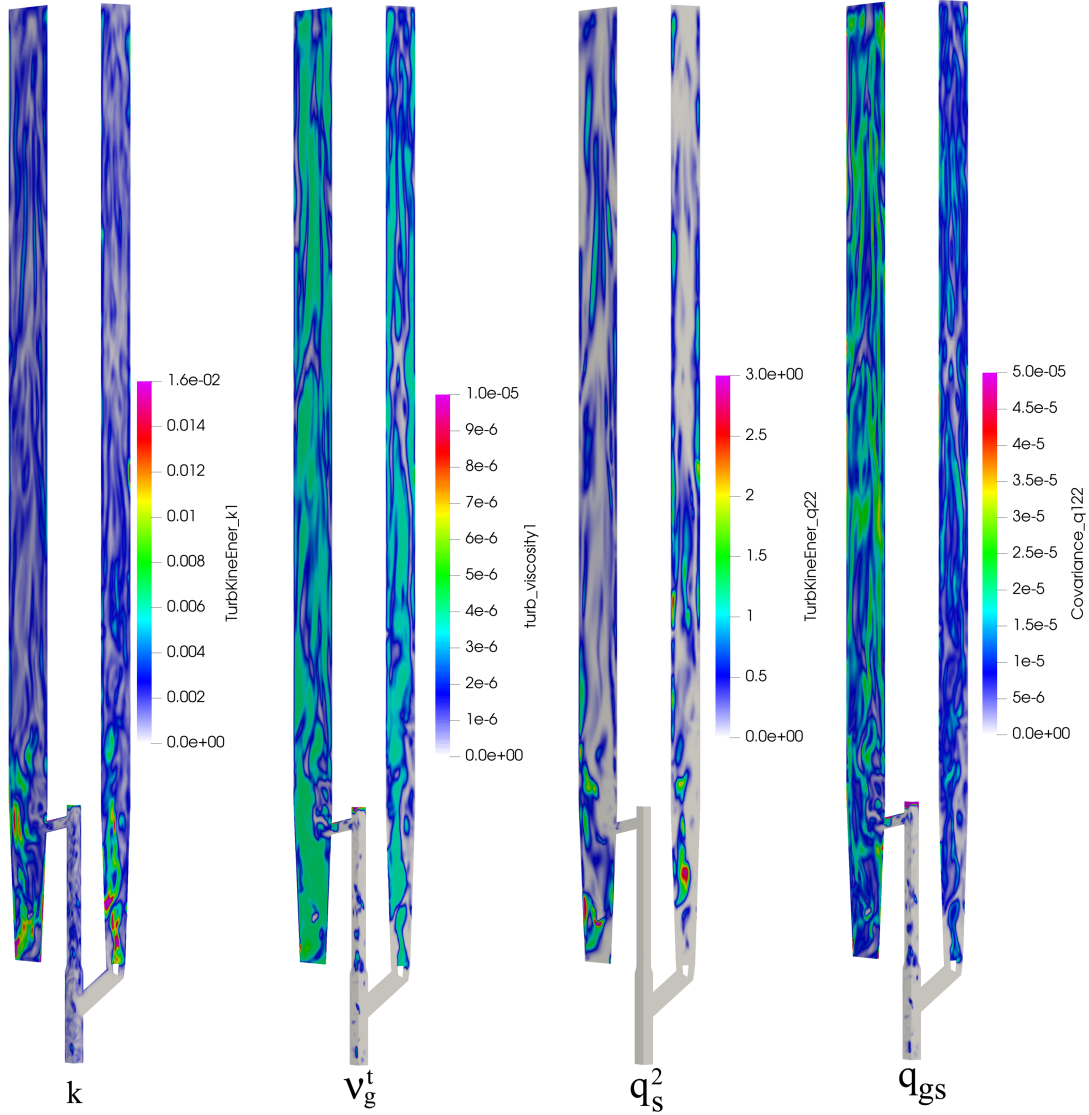


Figure 21: Instantaneous visualization of gas kinetic energy, gas turbulent viscosity, particle fluctuant kinetic energy and gas-particle velocity covariance.

690 suitable compromise between fine and coarse meshes, considering both the accuracy and com-
 691 putational costs. Results about the pressure in the different parts of the pilot showed a general
 692 agreement between numerical predictions and experimental data, proving that the simplifying
 693 assumptions considered in this study allow to reproduce satisfactorily the flow regime. The
 694 hydrodynamics of the process was therefore investigated in detail, in particular studying the
 695 solid mass flow rates, the gas and solid velocities and the particle distribution in the relevant
 696 parts of the CLC system. Numerical simulations showed that the air reactor operates in a
 697 circulating bed regime, while the fuel reactor works in a mixed regime, in between a dense and
 698 a circulating fluidized bed. Numerical simulations also showed that the gas turbulence is neg-
 699 ligible at this operating condition and weakly correlated with the particle fluctuating motion.
 700 So, according to the modeling approach, agitation between neighboring particles was found
 701 rather uncorrelated and for these reasons, both the uncorrelated and correlated collision mod-
 702 els led to almost the same results. The effects of the two limit-case wall boundary conditions
 703 (free-slip and no-slip) for the mean particle velocity were also analyzed. According to the solid

704 circulation, it was found that a no-slip condition in the air reactor leads to an increase of the
705 global circulation rate. The reason is not completely understood. The asymmetry of the solid
706 velocity radial profiles in the air reactor makes the back-mixing analysis inconclusive at this
707 stage. Further studies are needed to clarify this point. The results however suggested that a
708 no-slip boundary condition can be considered satisfactory in a dense regime, but its use should
709 be avoided in dilute zones, such as in the air reactor. The question of the wall boundary condi-
710 tions for the solid phase is an important point that deserves to be investigated further, and it
711 is left as a future work. Indeed, more appropriate boundary conditions should be used to rep-
712 resent the behavior of the different particle-wall interactions in the presence of both dense and
713 dilute regimes. Globally, the current study assessed satisfactorily the isothermal, non-reactive
714 modeling approach regarding the hydrodynamic predictions of a reactive unit. This allows the
715 design phase to deal with the reactive aspects at a later time.

716 Acknowledgment

717 This work is supported by Chinese-European Emission-Reducing Solutions (CHEERS) un-
718 der the European Union’s Horizon 2020 research and innovation program (No 764697). For
719 the numerical simulations at IMFT, it was granted access to the HPC resources of CALMIP
720 supercomputing center under the allocation P19017 and CINES supercomputing center under
721 the allocation A0082B10864. CALMIP and CINES are gratefully acknowledged. The authors
722 wish to thank Ing. Hervé Neau (CoSiNus) for his help with the NEPTUNE_CFD code.

723 Nomenclature

Latin Symbols

| | |
|-----------------|------------------------------------|
| C_D | drag coefficient |
| d_s | particle diameter |
| $D_{s,ij}$ | particle shear tensor |
| e_c | normal restitution coefficient |
| g | gravity |
| g_0 | radial distribution function |
| I | interphase momentum transfer |
| k | gas turbulent kinetic energy |
| P | pressure |
| P_s^{fr} | frictional pressure |
| q_{gs} | fluid-particle velocity covariance |
| q_s^2 | particle fluctuant kinetic energy |
| \tilde{q}_s^2 | correlated particle kinetic energy |
| $R_{g,ij}$ | turbulent-Reynolds stress tensor |
| Re_p | particle Reynolds number |
| $R_{s,ij}$ | particle kinetic stress tensor |
| u'' | velocity fluctuation |
| U | mean velocity |
| v_r | instantaneous relative velocity |
| V_r | relative velocity |
| V_d | drift velocity |

Greek letters

| | |
|-------------------------------------|----------------------------------------------------------|
| α | volume fraction |
| δ_{ij} | Kronecker symbol |
| δq_s^2 | uncorrelated contribution of the particle kinetic energy |
| ε | gas turbulent dissipation rate |
| ε_{gs} | fluid-particle covariance dissipation rate |
| ζ_{gs}^2 | correlation coefficient |
| η | internal friction angle |
| Θ_s | granular temperature |
| $\Theta_{g,ij}$ | viscous stress tensor |
| $\Theta_{s,ij}$ | collisional stress tensor |
| κ_s^{eff} | particle effective diffusivity |
| κ_s^{kin} | particle kinetic diffusivity |
| κ_s^{col} | particle collisional diffusivity |
| μ_g | laminar dynamic viscosity |
| μ_s^{fr} | frictional viscosity |
| ν_g^t | turbulent kinematic viscosity |
| ν_s^{kin} | particle kinetic viscosity |
| ν_s^{col} | particle collisional viscosity |
| ν_{gs}^t | turbulent gas-particle viscosity |
| Π_{qgs} | interphase gas-particle covariance interaction term |
| Π_{qs} | interphase turbulent kinetic energy transfer rate |
| $\Pi_{s \rightarrow g}^k$ | interphase turbulent kinetic energy interaction term |
| $\Pi_{s \rightarrow g}^\varepsilon$ | interphase turbulent dissipation rate interaction term |
| ρ | density |
| $\sum_{,ij}$ | stress tensor |
| τ_g^t | fluid turbulent time scale |
| τ_{gs}^t | eddy-particle interaction time |
| τ_{gs}^F | mean particle relaxation time |
| τ_s^c | inter-particle collision time |
| $\phi_{s,ij}$ | frictional tensor |

Abbreviation

| | |
|------|-----------------------------------------|
| AR | air reactor |
| CFB | circulating fluidized bed |
| CFD | computational fluid dynamics |
| CLC | chemical looping combustion |
| CLOU | chemical looping with oxygen uncoupling |
| DEM | Discrete Element Method |
| EMMS | energy minimization multi-scale |
| FR | fuel reactor |
| HPC | high performance computing |
| OC | oxygen carrier |

724 References

- 725 Abad, A., Adánez, J., Cuadrat, A., García-Labiano, F., Gayán, P., de Diego, L. F., 2011.
726 Kinetics of redox reactions of ilmenite for chemical-looping combustion. *Chemical Engineering*
727 *Science* 66 (4), 689–702.

- 728 Abad, A., Gayán, P., Pérez-Vega, R., García-Labiano, F., de Diego, L., Mendiara, T., Izquierdo,
729 M., Adánez, J., 2020. Evaluation of different strategies to improve the efficiency of coal
730 conversion in a 50 kWth chemical looping combustion unit. *Fuel* 271, 117514.
- 731 Abad, A., Pérez-Vega, R., de Diego, L. F., García-Labiano, F., Gayán, P., Adánez, J., 2015.
732 Design and operation of a 50 kWth Chemical Looping Combustion (CLC) unit for solid fuels.
733 *Applied Energy* 157, 295 – 303.
- 734 Bennani, L., Neau, H., Baudry, C., Laviéville, J., Fede, P., Simonin, O., 2017. Numerical
735 simulation of unsteady dense granular flows with rotating geometries. *Chemical Engineering*
736 *Research and Design* 120, 333 – 347.
- 737 Berguerand, N., Lyngfelt, A., 2008. Design and operation of a 10 kWth chemical-looping com-
738 bustor for solid fuels – Testing with South African coal. *Fuel* 87 (12), 2713 – 2726.
- 739 Boelle, A., Balzer, G., Simonin, O., 1995. Second-order prediction of the particle-phase stress
740 tensor of inelastic spheres in simple shear dense suspensions. *American Society of Mechanical*
741 *Engineers, Fluids Engineering Division (Publication) FED* 228, 9–18.
- 742 Cao, Y., Casenas, B., Pan, W.-P., 2006. Investigation of chemical looping combustion by solid
743 fuels. 2. Redox reaction kinetics and product characterization with coal, biomass, and solid
744 waste as solid fuels and CuO as an oxygen carrier. *Energy & Fuels* 20 (5), 1845–1854.
- 745 Chen, X., Ma, J., Tian, X., Wan, J., Zhao, H., 2019. CPFD simulation and optimization of
746 a 50 kWth dual circulating fluidized bed reactor for chemical looping combustion of coal.
747 *International Journal of Greenhouse Gas Control* 90, 102800.
- 748 Cloete, S., Johansen, S. T., Amini, S., 2012. Performance evaluation of a complete lagrangian
749 KTGF approach for dilute granular flow modelling. *Powder Technology* 226, 43–52.
- 750 Cundall, P. A., Strack, O. D. L., 1979. A discrete numerical model for granular assemblies.
751 *Géotechnique* 29 (1), 47–65.
- 752 Di Renzo, A., Napolitano, E. S., Di Maio, F. P., 2021. Coarse-grain DEM modelling in fluidized
753 bed simulation: A review. *Processes* 9 (2).
- 754 EDF R&D, 2017. NEPTUNE_CFD Version 4.0.1 User Guide. EDF R&D, Fluid Dynamics,
755 Power Generation and Environment Department, Multi-Phase en Reactive Flow Group, 6
756 Quai Watier, 78401 Chatou CEDEX, France.
- 757 Fede, P., Simonin, O., Ingram, A., 2016. 3D numerical simulation of a lab-scale pressurized
758 dense fluidized bed focussing on the effect of the particle-particle restitution coefficient and
759 particle-wall boundary conditions. *Chemical Engineering Science* 142, 215–235.
- 760 Février, P., Simonin, O., Squires, K. D., 2005. Partitioning of particle velocities in gas–solid
761 turbulent flows into a continuous field and a spatially uncorrelated random distribution:
762 theoretical formalism and numerical study. *Journal of Fluid Mechanics* 533, 1–46.
- 763 Fox, R. O., 2014. On multiphase turbulence models for collisional fluid–particle flows. *Journal*
764 *of Fluid Mechanics* 742, 368–424.
- 765 Gidaspow, D., 1994. In: *Multiphase flow and fluidization: continuum and kinetic theory de-*
766 *scriptions*. Academic press, San Diego.

- 767 Gobin, A., Neau, H., Simonin, O., Llinas, J., Reiling, V., Sélo, J., 2003. Fluid dynamic numerical
768 simulation of a gas phase polymerization reactor. *International Journal for Numerical*
769 *Methods in Fluids* 43 (10-11), 1199–1220.
- 770 Goniva, C., Kloss, C., Deen, N. G., Kuipers, J. A., Pirker, S., 2012. Influence of rolling friction
771 on single spout fluidized bed simulation. *Particuology* 10 (5), 582–591.
- 772 Hamidouche, Z., Masi, E., Fede, P., Ansart, R., Neau, H., Hemati, M., Simonin, O., 2018.
773 Chapter two - numerical simulation of multiphase reactive flows. In: *Bridging Scales in*
774 *Modelling and Simulation of Non-Reacting and Reacting Flows. Part I. Vol. 52 of Advances*
775 *in Chemical Engineering*. Academic Press, pp. 51–124.
- 776 Hamidouche, Z., Masi, E., Fede, P., Simonin, O., Mayer, K., Penthor, S., 2019. Unsteady
777 three-dimensional theoretical model and numerical simulation of a 120-kW chemical looping
778 combustion pilot plant. *Chemical Engineering Science* 193, 102–119.
- 779 Haus, J., Lindmüller, L., Dymala, T., Jarolin, K., Feng, Y., Hartge, E.-U., Heinrich, S., Werther,
780 J., 2020. Increasing the efficiency of chemical looping combustion of biomass by a dual-stage
781 fuel reactor design to reduce carbon capture costs. *Mitigation and Adaptation Strategies for*
782 *Global Change* 25 (6), 969–986.
- 783 Igci, Y., Sundaresan, S., 2011a. Constitutive models for filtered two-fluid models of fluidized
784 gas–particle flows. *Industrial & Engineering Chemistry Research* 50 (23), 13190–13201.
- 785 Igci, Y., Sundaresan, S., 2011b. Verification of filtered two-fluid models for gas-particle flows
786 in risers. *AIChE Journal* 57 (10), 2691–2707.
- 787 Jenkins, J. T., Richman, M. W., 1986. Grad’s 13-moment system for a dense gas of inelastic
788 spheres. In: *The Breadth and Depth of Continuum Mechanics*. Springer Berlin Heidelberg,
789 Berlin, Heidelberg, pp. 647–669.
- 790 Johnson, P. C., Jackson, R., 1987. Frictional-collisional constitutive relations for granular ma-
791 terials, with application to plane shearing. *Journal of Fluid Mechanics* 176, 67–93.
- 792 Johnson, P. C., Nott, P., Jackson, R., 1990. Frictional-collisional equations of motion for par-
793 ticipate flows and their application to chutes. *Journal of Fluid Mechanics* 210, 501–535.
- 794 Kim, H. R., Wang, D., Zeng, L., Bayham, S., Tong, A., Chung, E., Kathe, M. V., Luo, S.,
795 McGiveron, O., Wang, A., Sun, Z., Chen, D., Fan, L., 2013. Coal direct chemical looping
796 combustion process: Design and operation of a 25-kWth sub-pilot unit. *Fuel* 108, 370–384.
- 797 Kolehmainen, J., Ozel, A., Sundaresan, S., 2018. Eulerian modelling of gas–solid flows with
798 triboelectric charging. *Journal of Fluid Mechanics* 848, 340–369.
- 799 Langørgen, Ø., Saanum, I., Haugen, N. E. L., 2017. Chemical looping combustion of methane
800 using a copper-based oxygen carrier in a 150 kW reactor system. *Energy Procedia* 114, 352
801 – 360.
- 802 Laviéville, J., Deutsch, E., Simonin, O., 1995. Large eddy simulation of interactions between
803 colliding particles and a homogeneous isotropic turbulence field. *American Society of Me-*
804 *chanical Engineers, Fluids Engineering Division (Publication) FED* 228, 347–357.

- 805 Leion, H., Mattisson, T., Lyngfelt, A., 2008. Solid fuels in chemical-looping combustion. Inter-
806 national Journal of Greenhouse Gas Control 2 (2), 180–193.
- 807 Li, J., Kwauk, M., 1994. Particle-fluid two-phase flow : The Energy-Minimization Multi-Scale
808 Method. Metallurgical Industry Press, Beijing, China.
- 809 Li, J., Zhang, H., Gao, Z., Fu, J., Ao, W., Dai, J., 2017. CO₂ capture with chemical looping
810 combustion of gaseous fuels: An overview. Energy & Fuels 31 (4), 3475–3524.
- 811 Linderholm, C., Schmitz, M., Knutsson, P., Lyngfelt, A., 2016. Chemical-looping combustion
812 in a 100-kW unit using a mixture of ilmenite and manganese ore as oxygen carrier. Fuel 166,
813 533–542.
- 814 Lyngfelt, A., 2014. Chemical-looping combustion of solid fuels – status of development. Applied
815 Energy 113, 1869 – 1873.
- 816 Lyngfelt, A., Leckner, B., Mattisson, T., 2001. A fluidized-bed combustion process with inherent
817 CO₂ separation; application of chemical-looping combustion. Chemical Engineering Science
818 56 (10), 3101–3113.
- 819 Lyngfelt, A., Linderholm, C., 2017. Chemical-looping combustion of solid fuels – status and re-
820 cent progress. Energy Procedia 114, 371 – 386, 13th International Conference on Greenhouse
821 Gas Control Technologies, GHGT-13, 14-18 November 2016, Lausanne, Switzerland.
- 822 Ma, J., Tian, X., Wang, C., Chen, X., Zhao, H., 2018. Performance of a 50 kWth coal-fuelled
823 chemical looping combustor. International Journal of Greenhouse Gas Control 75, 98–106.
- 824 Mahalatkar, K., Kuhlman, J., Huckaby, E. D., O’Brien, T., 2011. CFD simulation of a chemical-
825 looping fuel reactor utilizing solid fuel. Chemical Engineering Science 66 (16), 3617–3627.
- 826 Markström, P., Linderholm, C., Lyngfelt, A., 2013. Chemical-looping combustion of solid fuels
827 – design and operation of a 100 kW unit with bituminous coal. International Journal of
828 Greenhouse Gas Control 15, 150 – 162.
- 829 Mattisson, T., Keller, M., Linderholm, C., Moldenhauer, P., Rydén, M., Leion, H., Lyngfelt,
830 A., 2018. Chemical-looping technologies using circulating fluidized bed systems: Status of
831 development. Fuel Processing Technology 172, 1–12.
- 832 May, J., Alobaid, F., Ohlemüller, P., Stroh, A., Ströhle, J., Epple, B., 2018. Reactive two-fluid
833 model for chemical-looping combustion – simulation of fuel and air reactors. International
834 Journal of Greenhouse Gas Control 76, 175 – 192.
- 835 Molodtsov, Y., 2003. Theoretical analysis of the flow regimes and their characteristics in verti-
836 cally flowing gas–solids suspensions. Chemical Engineering Journal 96 (1), 133–143.
- 837 Montilla, C., Ansart, R., Simonin, O., 2020. Modelling of the mean electric charge transport
838 equation in a mono-dispersed gas–particle flow. Journal of Fluid Mechanics 902, A12.
- 839 Neau, H., Pigou, M., Fede, P., Ansart, R., Baudry, C., Mériçoux, N., Laviéville, J., Fournier,
840 Y., Renon, N., Simonin, O., 2020. Massively parallel numerical simulation using up to 36,000
841 cpu cores of an industrial-scale polydispersed reactive pressurized fluidized bed with a mesh
842 of one billion cells. Powder Technology 366, 906 – 924.

- 843 Ozel, A., Fede, P., Simonin, O., 2013. Development of filtered Euler–Euler two-phase model
844 for circulating fluidised bed: High resolution simulation, formulation and a priori analyses.
845 *International Journal of Multiphase Flow* 55, 43–63.
- 846 Parker, J. M., 2014. CFD model for the simulation of chemical looping combustion. *Powder*
847 *Technology* 265, 47–53.
- 848 Parmentier, J.-F., Simonin, O., Delsart, O., 2012. A functional subgrid drift velocity model for
849 filtered drag prediction in dense fluidized bed. *AIChE Journal* 58 (4), 1084–1098.
- 850 Penthor, S., Stollhof, M., Pröll, T., Hofbauer, H., 2016. Detailed fluid dynamic investigations of
851 a novel fuel reactor concept for chemical looping combustion of solid fuels. *Powder Technology*
852 287, 61–69.
- 853 Pérez-Astray, A., Mendiara, T., de Diego, L., Abad, A., García-Labiano, F., Izquierdo, M.,
854 Adánez, J., 2020. Improving the oxygen demand in biomass CLC using manganese ores. *Fuel*
855 274, 117803.
- 856 Pérez-Vega, R., Abad, A., Gayán, P., García-Labiano, F., Izquierdo, M. T., de Diego, L. F.,
857 Adánez, J., 2020. Coal combustion via Chemical Looping assisted by Oxygen Uncoupling
858 with a manganese-iron mixed oxide doped with titanium. *Fuel Processing Technology* 197,
859 106184.
- 860 Pirker, S., Kahrimanovic, D., Kloss, C., Popoff, B., Braun, M., 2010. Simulating coarse particle
861 conveying by a set of Eulerian, Lagrangian and hybrid particle models. *Powder Technology*
862 204 (2), 203–213.
- 863 Pröll, T., Kolbitsch, P., Bolhàr-Nordenkampf, J., Hofbauer, H., 2009. A novel dual circulating
864 fluidized bed system for chemical looping processes. *AIChE Journal* 55 (12), 3255–3266.
- 865 Reinking, Z., Shim, H.-S., Whitty, K. J., Lighty, J. S., 2019. Computational simulation of a 100
866 kW dual circulating fluidized bed reactor processing coal by chemical looping with oxygen
867 uncoupling. *International Journal of Greenhouse Gas Control* 90, 102795.
- 868 Schneiderbauer, S., Pirker, S., 2014. Filtered and heterogeneity-based subgrid modifications for
869 gas–solid drag and solid stresses in bubbling fluidized beds. *AIChE Journal* 60 (3), 839–854.
- 870 Shao, Y., Agarwal, R. K., Wang, X., Jin, B., 2020. Numerical simulation of a 3D full loop iG-
871 CLC system including a two-stage counter-flow moving bed air reactor. *Chemical Engineering*
872 *Science* 217, 115502.
- 873 Shao, Y., Agarwal, R. K., Wang, X., Jin, B., 2021. Review of computational fluid dynamics
874 studies on chemical looping combustion. *Journal of Energy Resources Technology* 143 (8),
875 080802.
- 876 Shen, L., Wu, J., Xiao, J., Song, Q., Xiao, R., 2009. Chemical-looping combustion of biomass
877 in a 10 kWth reactor with iron oxide as an oxygen carrier. *Energy & Fuels* 23 (5), 2498–2505.
- 878 Simonin, O., 2000. Statistical and continuum modelling of turbulent reactive particulate flows.
879 part 1: Theoretical derivation of dispersed Eulerian modelling from probability density func-
880 tion kinetic equation. In: *Lecture Series. Vol. 6 of Theoretical and Experimental Modeling of*
881 *Particulate Flows.* von Karman Institute for Fluid Dynamics Rhode Saint Genèse, Belgium.

- 882 Simonin, O., Deutsch, E., Minier, J. P., 1993. Eulerian prediction of the fluid/particle correlated
883 motion in turbulent two-phase flows. *Applied Scientific Research* 51, 275–283.
- 884 Simonin, O., Février, P., Laviéville, J., 2002. On the spatial distribution of heavy-particle
885 velocities in turbulent flow: from continuous field to particulate chaos. *Journal of Turbulence*
886 3, N40.
- 887 Siriwardane, R., Tian, H., Richards, G., Simonyi, T., Poston, J., 2009. Chemical-looping com-
888 bustion of coal with metal oxide oxygen carriers. *Energy & Fuels* 23 (8), 3885–3892.
- 889 Snider, D., 2001. An incompressible three-dimensional multiphase particle-in-cell model for
890 dense particle flows. *Journal of Computational Physics* 170 (2), 523–549.
- 891 Srivastava, A., Sundaresan, S., 2003. Analysis of a frictional–kinetic model for gas–particle
892 flow. *Powder Technology* 129 (1), 72–85.
- 893 Ströhle, J., Orth, M., Epple, B., 2014. Design and operation of a 1 MWth chemical looping
894 plant. *Applied Energy* 113, 1490–1495.
- 895 Ströhle, J., Orth, M., Epple, B., 2015. Chemical looping combustion of hard coal in a 1 MWth
896 pilot plant using ilmenite as oxygen carrier. *Applied Energy* 157, 288–294.
- 897 Su, M., Zhao, H., Ma, J., 2015. Computational fluid dynamics simulation for chemical looping
898 combustion of coal in a dual circulation fluidized bed. *Energy Conversion and Management*
899 105, 1–12.
- 900 Thon, A., Kramp, M., Hartge, E.-U., Heinrich, S., Werther, J., 2014. Operational experience
901 with a system of coupled fluidized beds for chemical looping combustion of solid fuels using
902 ilmenite as oxygen carrier. *Applied Energy* 118, 309 – 317.
- 903 Thunman, H., Niklasson, F., Johnsson, F., Leckner, B., 2001. Composition of volatile gases and
904 thermochemical properties of wood for modeling of fixed or fluidized beds. *Energy & Fuels*
905 15 (6), 1488–1497.
- 906 Tsuji, Y., Kawaguchi, T., Tanaka, T., 1993. Discrete particle simulation of two-dimensional
907 fluidized bed. *Powder Technology* 77 (1), 79–87.
- 908 Vermorel, O., Bédard, B., Simonin, O., Poinso, T., 2003. Numerical study and modelling of
909 turbulence modulation in a particle laden slab flow. *Journal of Turbulence* 4 (25), 1–39.
- 910 Wang, J., van der Hoef, M. A., Kuipers, J. A. M., 2009. Why the two-fluid model fails to predict
911 the bed expansion characteristics of Geldart A particles in gas-fluidized beds: A tentative
912 answer. *Chemical Engineering Science* 64 (3), 622 – 625.
- 913 Wang, S., Lu, H., Zhao, F., Liu, G., 2014. CFD studies of dual circulating fluidized bed reactors
914 for chemical looping combustion processes. *Chemical Engineering Journal* 236, 121–130.
- 915 Wang, X., Shao, Y., Jin, B., Zhang, Y., 2020a. Three-dimensional multiphase full-loop simu-
916 lation of directional separation of binary particle mixtures in high-flux coal-direct chemical-
917 looping combustion system. *Particuology* 49, 179 – 190.
- 918 Wang, X., Wang, X., Shao, Y., Jin, B., 2020b. Three-dimensional modelling of the multiphase
919 hydrodynamics in a separated-gasification chemical looping combustion unit during full-loop
920 operation. *Journal of Cleaner Production* 275, 122782.

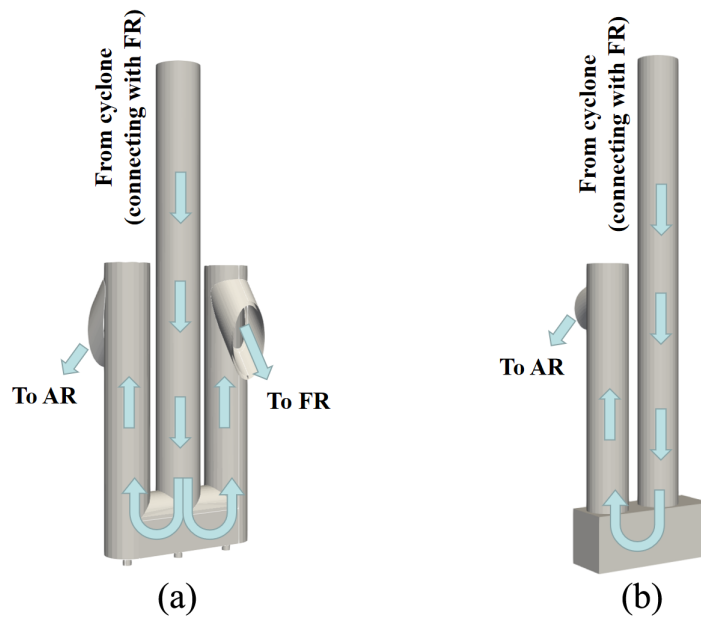


Figure A.22: FR loop-seal scheme: original sketch accounting for three chambers (left); numerical simulation (right).

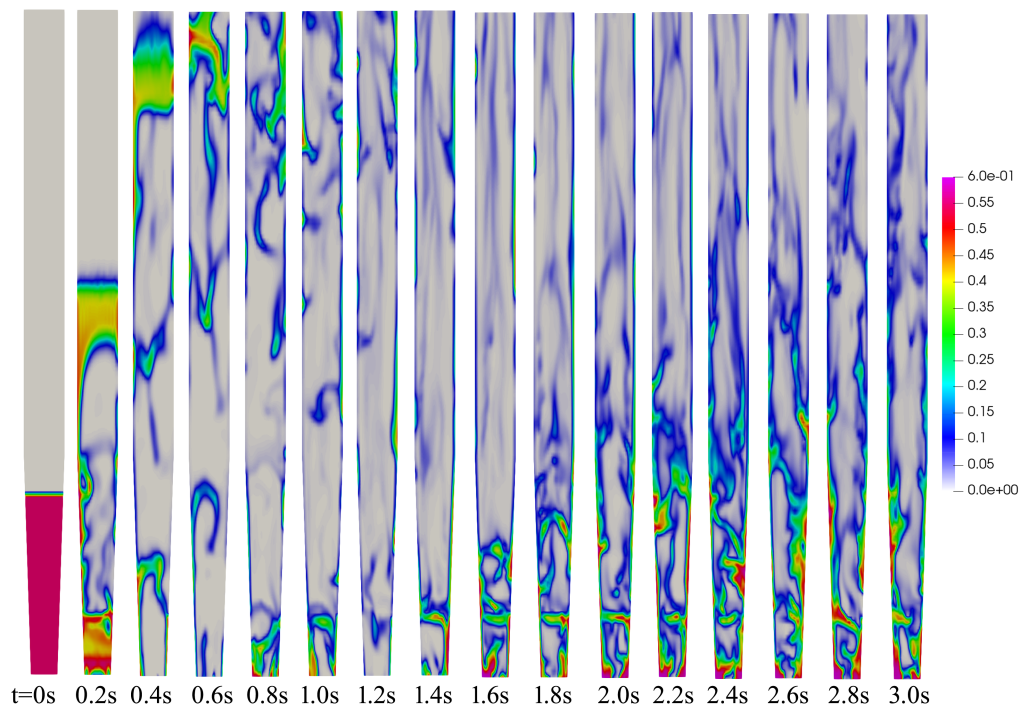


Figure A.23: Instantaneous solid volume fraction in a middle plane within the fuel reactor at the beginning stage of the simulation.